Cryo-ET of infected cells reveals that a succession of two lattices drives vaccinia virus assembly

Miguel Hernandez-Gonzalez[1], Thomas Calcraft[2], Andrea Nans[3], Peter B Rosenthal[2] and Michael Way[1, 4] *

[1]Cellular signalling and cytoskeletal function laboratory, The Francis Crick Institute, 1 Midland Road, London, NW1 1AT, UK

[2]Structural Biology of Cells and Viruses Laboratory, The Francis Crick Institute.

[3]Structural Biology Science Technology Platform, The Francis Crick Institute.

[4] Department of Infectious Disease, Imperial College, London W2 1PG, UK

*To whom correspondence should be addressed. Email: michael.way@crick.ac.uk

Running title: Cryo-ET of vaccinia infected cells

Abstract

During its cytoplasmic replication, vaccinia virus assembles non-infectious spherical immature virions (IV) coated by a viral D13 lattice. Subsequently, IV mature into infectious brick-shaped intracellular mature virus (IMV) that lack D13. Here, we performed cryo-electron tomography of frozen-hydrated vaccinia-infected cells to structurally characterise the maturation process in situ. During IMV formation a new pseudohexagonal lattice forms inside IV to produce the viral core. This lattice, consisting of trimeric pillars, appears as a palisade in cross-section. Our measurements suggest that the length of this core is determined by the D13 lattice. During maturation, which involves a 50% reduction in volume, the viral membrane becomes corrugated as it adapts to the IMV core in a process that does not appear to require membrane removal. Our study suggests that the flexible viral membrane is controlled by the consecutive D13 and palisade lattices, which structurally define vaccinia assembly and maturation.

Significance statement

Poxviruses such as variola virus (smallpox) and monkeypox induce disease in humans. Other poxviruses, including vaccinia virus and modified vaccinia Ankara (MVA), are used as vaccine vectors. Despite their importance, a structural understanding of how infectious poxvirus virions assemble in the cytoplasm of infected cells is lacking. In this study, we used cryo-electron tomography of frozen-hydrated vaccinia infected cells to structurally characterise the maturation of spherical immature virions into the infectious brick-shaped intracellular mature virus. These high-resolution in situ observations reveal new features concerning the viral membrane and the inner core of mature virions. The model that emerges suggests that two consecutive viral-derived protein lattices drive vaccinia assembly and maturation.

73 **Introduction**

74 Poxviruses are large double stranded DNA viruses that replicate and assemble their virions
75 in cytoplasmic perinuclear viral factories (1). The family includes variola virus, the causative
76 agent of smallpox, and monkeypox as well as vaccinia, the most studied family member
77 which was used as the vaccine to eradicate smallpox (2, 3). During its replication cycle,
78 vaccinia initially assembles into infectious intracellular mature virions (IMV), which are
79 released when infected cells lyse (4). Prior to cell lysis, however, some IMV become
80 enveloped by a Golgi cisterna or endosomal compartment to form intracellular enveloped
81 virions (IEV) (5-7) (Figure 1A). IEV undergo kinesin-1 mediated microtubule transport to the
82 plasma membrane, where they fuse to release extracellular enveloped virions (EEV) that
83 promote the long-range spread of infection (8, 9). Alternatively, after fusion some virions
84 (cell-associated enveloped virus, CEV) remain attached to the cell to stimulate actin-
85 dependent cell-to-cell spread of the virus (10-13).

86

87 The first step in the spread of vaccinia infection is the assembly of IMV, which are the
88 precusor to all subsequent forms (IEV, EEV and CEV) of the virus. IMV formation is initiated
89 when endoplasmic reticulum (ER) associated viral membrane assembly proteins (VMAPs)
90 promote the formation of isolated membrane crescents in the cytoplasm of infected cells
91 (14-16). The characteristic shape of the crescents is determined and maintained by the D13
92 scaffolding viral protein, which forms trimers that assemble into a hexameric lattice coating
93 the outer surface of the membrane (14, 15, 17, 18). In vitro structural analysis of
94 recombinant D13 reveals it has a double-jelly-roll structure composed of 8 antiparallel ß-
95 strands that self assembles into a honeycomb lattice of pseudo-hexagonal trimers (19-22).
96 Ultimately, membrane crescents develop into spherical immature virions (IV) which
97 encapsidate the viral genome and proteins required to produce an IMV (15, 17, 18, 23). In a
98 process that is still not understood but involves the proteolytic cleavage of viral proteins
99 and the formation of disulphide bonds, spherical IV undergo a dramatic reorganization into
100 brick-shaped IMV (24, 25). During this maturation process, the D13 honeycomb lattice is
101 lost, and a biconcave viral core assembles around the viral genome (23). The outer layer of
102 the viral core forms a paracrystalline palisade-like structure that has been reported to be
103 discontinuous (23, 26, 27). In addition, two dense proteinaceous aggregates, known as the
104 lateral bodies, assemble in the cavity between the outer viral membrane and the biconcave
105 viral core (23, 26, 28).

106

107 Vaccinia virion assembly has been extensively studied. Nevertheless, the key structural
108 determinants that govern the changes occurring during the IV to IMV transistion as well as

109 those that define the IMV remain unknown. To obtain detailed ultra-structural insights into
110 this maturation process, we have now performed cryo-electron tomography (cryo-ET) of
111 vaccinia infected cells. Our analysis reveals that a succession of two different viral lattices
112 drives assembly of IMV: D13 shapes the IV membrane, which subsequently coalesces onto
113 the pseudohexagonal palisade lattice, which is reminiscent of a viral capsid.
114
115 **Results**
116 **Electron cryo-tomography of vaccinia virus in infected cells**
117 Cryo-tomograms of thin cellular regions containing IV and IMV were recorded from the
118 periphery of HeLa cells infected with vaccinia virus for 8 hours (Figure 1B, C and S1, Movie
119 1 and 2). IV, fully coated by the viral D13 lattice, are largely spherical and have a diameter
120 of 351.89 ± 2.88 nm (Table S1). Analysis of tomograms in 3D, however, reveals that a
121 proportion of IV despite being closed and fully coated by D13 have a single invagination of
122 the viral membrane (Figure 1B). This suggests that the D13 lattice is flexible and can
123 accommodate both positive and negative curvatures present on virions with invaginations.
124 This D13 lattice flexibility is also evident from its ability to coat the exterior of "open
125 spheres" with different membrane curvature (also known as crescents due to their shape
126 when seen in a middle view) during IV formation (Figure 2A, B and Movie 3).
127
128 The interior of the majority of IV, which contain viral DNA and proteins required for virion
129 assembly, are homogenous and lack any of the distinctive regions or layers seen in IMV
130 (Figure 1B). In a few cases, however, we could observe a single dense striated structure
131 inside IV corresponding to the nucleoid (viral DNA genome) before it decondenses (Figure
132 2C and S2), as seen in previous ultra-structural analysis of thin EM sections of vaccinia
133 infected cells (28). We also found examples of related striated structures in the cytoplasm
134 adjacent to, or in direct association with, assembling IV (Figure 2D, E). Consistent with the
135 interpretation that the example shown in Figure 2E represents the viral genome being
136 inserted into assembling IV, structured illumination microscopy together with deconvolution
137 (125 nm resolution) also reveals the presence of elongated DNA structures associating with
138 virions, identified by RFP-A3, in the viral factory (Figure 2F). Our 3D tomographic
139 observations of assembling IV using cryo-ET were consistent with previous ultra-structural
140 analysis of vaccinia infected cells using electron microscopy (16-18, 29, 30).
141
142 **In situ structure of the hexagonal D13 lattice**
143 Structural analysis of recombinant D13 in isolation has provided a detailed molecular
144 understanding of the D13 trimer (19-22). However, the macromolecular arrangements of

145 the D13 lattice on IV in infected cells have largely been studied by deep-etch EM (17, 18).
146 Given the clear lattices present on the IV surface in our tomograms (Figure 3A, Movie 4), we
147 analysed the structure of the D13 lattice in situ by subtomogram averaging. We obtained
148 maps by averaging surface sectors revealing hexamers of trimer arrangements with a lattice
149 spacing of 133 Å, in agreement with lattices described for in vitro assembled D13 and deep-
150 etch EM honeycombs (Figure 3B). Rigid-body docking of the high-resolution structure of a
151 D13 trimer (PDB: 7VFE) into the map shows the packing of D13 trimers is consistent with
152 that recently reported (19). While at much lower resolution, precluding a detailed
153 description of interface residues, the arrangement of D13 on the spherical IV surface does
154 not appear to include a relative twist of trimeric axes between adjacent trimers as observed
155 in single particle dimers or tubular assembles.
156
157 From the hexagonal packing of D13 in the subtomogram average, we estimate that ~5,300
158 D13 trimers will cover the surface of a spherical IV. The packing density and radius of the
159 D13 lattice on IV are compatible with an icosahedrally symmetric architecture with a
160 triangulation number (T) in the neighborhood of 268. We have not confirmed the presence
161 of icosahedral symmetry, which would require pentameric arrangements of D13 trimers,
162 such as those that have been identified in vitro (19). Finally, we observed a gap of ~5.6 nm
163 between the innermost surface of the D13 lattice and the membrane of the IV. This gap
164 cannot be explained by any unresolved N- or C-terminal residues of D13 and must therefore
165 be bridged by another protein such as A17 (21).
166
167 **Structure of intracellular mature virus in infected cells**
168 The internal organisation, dimensions and shape of IMV, which are "brick-shaped"
169 membrane-bound virions, contrast dramatically with those of IV (Figure 1). Analysis of the
170 size and shape of IMV in 3D reveals they can be approximated to a triaxial ellipsoid of 352 x
171 281 x 198 nm with a calculated volume of 1.02 x 10^7 nm^3 (Figure 4, Table S1 & Movie 5).
172 The outer membrane of IMV has a corrugated appearance and the D13 lattice is absent.
173 There is, however, a new additional outer layer of 6.67 ± 0.11 nm on the viral membrane
174 that was not present on IV (Figure 4). Underneath the viral membrane there is a palisade-
175 looking structure consisting of a series of turret-like densities in cross-section (12.5 nm
176 thick) that is associated with a inner wall that is 3.84 ± 0.09 nm thick (Figure 4A). Depending
177 on the orientation of the virion, the interior organisation of the IMV appears very different.
178 In the mid view of its two widest dimensions (352 x 281 nm), the palisade appears in contact
179 with the viral membrane. However, in the orthogonal lateral view (352 x 198 nm) the
180 palisade structure, which only contacts the viral membrane at the ends of the virion (Figure

181 4B), forms a dumbbell shape that results in the formation of two concavities. Each cavity
182 contains a single dense and amorphous structure corresponding to a lateral body. The space
183 between the viral membrane and the palisade varies between 9.28 ± 0.18 nm and 46.53 ±
184 2.72 nm, the latter being where the lateral bodies are accommodated (see Table S1 for
185 detailed measurements). 3D tomographic analyses reveal that the palisade is a semi-regular
186 array when viewed from above (Figure 4C, D).
187
188 The semi-regular organisation of the palisade is most apparent in naked cores, which lack
189 the viral membrane and are occasionally found in the cytoplasm (Figure 5A, B).
190 Segmentation of our 3D tomograms reveals the palisade is a continuous structure without
191 fenestrations that defines the virus core, including the regions that contact the lateral
192 bodies (Figure 4E, Movie 6). Inside the core, there are no obvious higher order structures.
193 There are, however, interconnected densities that vary between virions but tend to
194 accumulate beneath the inner wall of the core (Figure 4A). These densities are especially
195 apparent in the compressed region underneath the lateral bodies (Figure 4C). Such densities
196 associated with the inner wall of the core potentially represent the viral genome and its
197 associated proteins given its high contrast. Another characteristic that is evident in
198 midplane views of approximately half of the IMV (48.9%, n = 94), is that one corner of the
199 virion (and in a few cases, two corners) appears as a straight or flattened "cut corner"
200 (Figure 1C and Figure S3). This characteristic is intrinsic to the core wall as it is also apparent
201 in naked cores (Figure 5A, Movie 7) and has been previously observed in purified cores (27).
202 In addition, these naked cores lack the two densities corresponding to lateral bodies but
203 have associated spaghetti-like structures contacting the palisade surface (Figure 5A). These
204 flexible polymers, which are 2.6 nm in diameter, form an exclusion zone of ~ 40 nm around
205 the naked core (Figure 5A). Furthermore, it was noticeable that naked cores have randomly
206 distributed ring like structures on their surface that were not observed in IMV. These rings
207 seem to protrude 10-20 nm from the palisade surface and had inner and outer diameters of
208 4.5 ± 0.1 nm and 9.9 ± 0.1 nm, respectively (Figure 5C).
209
210 **The distinct hexagonal core lattice of infectious vaccinia virions**
211 During viral egress, some IMV become triple-membraned intracellular enveloped virions
212 (IEV) after envelopment by a Golgi cisterna or endosomal compartment (Figure 1A).
213 Subsequent fusion of the IEV with the plasma membrane liberates double-membraned
214 extracellular enveloped virions (EEV) that are known as cell-associated extracellular
215 enveloped virions (CEV) if they remain attached to the outside of the cell (7). Our
216 tomograms reveal that the additional membranes acquired by envelopment are not

217 corrugated (Figure 6A). In the case of IEV, the outer membrane is also not always in close
218 contact with the underlying membrane (see Table S1 for virion measurements). The
219 dimensions and structure of the IMV are also unaffected by envelopment (Figure 6A).
220 Notably, the palisade fully coats the viral core in all infectious virions and its organisation
221 appears unaltered (Figure 6A-C). To study the architecture of the palisade, we performed
222 subtomogram averaging separately using IMV, IEV and CEV/EEV particles. Maps obtained
223 from the different virion types, all displayed the same organisation and lattice parameters
224 (P6 symmetry with a=b=89 ± 2 Å, θ=120°) (Fig S4). A new combined map obtained by
225 averaging all particle types, reveals that the palisade is composed of trimeric pillars with
226 projecting lobes that interact with neighbouring pillars with local hexagonal symmetry
227 (Figure 6D). These pillars are embedded in an unfeatured inner wall. While further details
228 are required to understand its molecular composition, this arrangement appears to be
229 flexible enough to assemble a continuous biconcave capsid structure.
230
231 **Maturation of IV to IMV**
232 Radical changes in the organisation, dimensions and shape of IV result in the formation of
233 IMV (Figure 7). Based on our tomograms, IV have an average diameter of 351.89 ± 2.88 nm
234 and a volume of 2.28 x 10^7 nm^3 for completely spherical particles (Figure 7A). In contrast,
235 "brick-shaped" IMV have a volume of 1.02 x 10^7 nm^3 based on dimensions of 352 x 281 x 198
236 nm (Figure 7A). This reduction in volume is accompanied by a dramatic corrugation of the
237 viral membrane, together with the loss of the D13 lattice. To better understand this
238 corrugation process, we measured the middle-plane perimeter of the viral membrane in IV
239 and IMV, following the wrinkles of the viral membrane to obtain its contour length. We
240 found that the membrane contour is virtually identical in IV and IMV, as well as in the
241 equivalent innermost mmembrane of EEV/CEV (~1100 nm, Figure 7B). This suggests the viral
242 membrane folds during maturation, which would explain the reduction in volume without
243 any detectable loss of membrane surface. In addition to reducing their volume by ~50%, IVs
244 also change their shape when they mature into IMV, becoming a triaxial ellipsoid. Strikingly,
245 the longest IMV dimension matches the diameter of IV (Figure 7A, B), suggesting that the
246 major axis of IMV is dictated by the IV diameter. In our tomograms we also found particles
247 that may represent intermediates and/or defective examples of IV maturation. These
248 include examples where the palisade is fully formed but the IV membrane, which either
249 lacks or is partially coated with D13, is not associated with the viral core (Figure 7C). It is
250 also interesting that we did not observe any virions with partially formed cores suggesting
251 that palisade formation is likely to be rapid or occurs en bloc.
252

253 **Discussion**

254 Previous ultra-structural analyses of vaccinia infected cells by electron microscopy over
255 many decades have provided important insights into the assembly of vaccinia virions. These
256 studies, however, have largely been conducted on fixed sections of infected cells which can
257 have fixation, processing and staining artifacts. Cryo-EM studies, analysing viral entry or
258 purified virions, have demonstrated the potential of using cryo-electron microscopy to study
259 vaccinia structure (26, 27, 31, 32). Here, we apply cryo-ET to image the thin edge of plunge-
260 frozen, vaccinia virus-infected cells, revealing virus architecture in situ. While there is
261 confirmation of past work, important new features emerged from our study. We found that
262 during maturation to IMV, spherical IV lose their D13-coat and reduce their volume by ~50%.
263 During this process, the outer viral membrane becomes corrugated when it associates with
264 the capsid-like palisade layer and the lateral bodies. The palisade, which remains unaltered
265 during subsequent virion morphogenesis, is a continuous regular lattice with
266 pseudohexagonal symmetry that fully covers the viral core. Our observations suggest that
267 these two lattices, D13 and the palisade, drive vaccinia assembly and maturation.
268
269 We found that the D13 lattices coating IV have a similar architecture to the D13 lattices
270 formed in vitro (19). Furthermore, Hyun et al. produced D13 spherical IV-like particles with
271 a similar diameter to the D13-coated IV we imaged in situ. This strongly suggests that the
272 D13 lattice, which initially curves open membranes and eventually forms closed particles,
273 determines both the size and shape of the IV. In addition, our images and STA maps show
274 that a 5.6-nm gap separates the D13 lattice from the IV membrane. This gap is most likely
275 occupied by A17, which tethers the D13 lattice to the membrane (21, 33, 34) but whose
276 flexibility would preclude its detection on the IV membrane by cryo-ET. The lack of direct
277 contact of the D13 protein lattice with the viral membrane is reminiscent of clathrin and
278 other vesicle-forming coats in eukaryotic cells where the structural lattice does not directly
279 interact with the membrane to be deformed (35, 36). Instead, an adaptor module mediates
280 the lattice-membrane association. A mechanism by which coat complexes promote
281 membrane curvature is by clustering the adaptor module on the membrane to be deformed
282 (37, 38). Therefore, D13-mediated clustering of A17 could promote membrane deformation
283 during IV formation. In addition, A17 can also contribute to membrane bending
284 independently of D13, since it can deform membranes in vitro and when expressed in non-
285 infected cells (39).
286
287 Despite their relatively constant diameter, a proportion of D13-coated IV have an elongated
288 membrane invagination (Figure 1A). This feature has largely gone unnoticed in previous EM

289 studies imaging thin sections, although IV membrane deformations are apparent in some
290 studies (28, 40-43). While the cause of this membrane buckling remains to be established,
291 it may relate to the thinness of the cell periphery or a consequence of forces on the
292 membrane during IV assembly or DNA insertion into assembling IV (42). As in other studies,
293 we observe the nucleoid in the IV interior or associated with either open or closed spheres,
294 as previously suggested for DNA entry events (28, 30). It is tempting to speculate that the
295 IV invagination may mark the site of DNA entry and IV sealing of the pore.
296 The palisade, which is largely composed of p4A and A4 (31, 44, 45), consists of a trimeric
297 assembly in a pseudo-hexagonal lattice arrangement. This new viral lattice, which fully
298 covers the core and defines its boundary, also dictates the dimensions and shape of IMV.
299 The viral membrane, no longer covered by D13, wrinkles and adopts the shape and
300 dimensions of the newly formed palisade. This process may also be responsible for the
301 compression of the lateral bodies onto the virus core, causing the biconcave deformation of
302 the latter. The maturation model that emerges from our work provides a simple way by
303 which a membrane-bound particle adapts to a new internal lattice and changes its shape
304 and dimensions to become more compact without membrane removal (Figure 7D).
305 Moreover, our data suggest the palisade length is dictated by the diameter of the IV, which
306 in turn is established by D13. The palisade would grow inside the D13-coated IV until
307 reaching its maximum length, that is the IV diameter. In other words, the D13 lattice limits
308 the longest dimension of the palisade lattice. The size restriction of a growing viral core by
309 its surrounding viral membrane has also been proposed for the assembly of the HIV core (46,
310 47). Our observation of a viral particle partly coated by D13 with an assembled palisade
311 suggests removal of D13 only occurs once the palisade is fully formed (Figure 7C). Moreover,
312 our observations suggest that palisade assembly and D13 removal are coordinated and rapid.
313
314 In the IMV, the lateral bodies define a lateral domain, as opposed to the virion tips, which
315 are specified by the long axis of the viral core. The lateral bodies prevent direct interactions
316 between the palisade and the wrinkled viral membrane, which may contribute to the
317 differences between the lateral and the tip domains. Notably, the virion tips are the site of
318 polarisation of the set of viral membrane proteins that form the entry fusion complex (EFC),
319 which is essential for virus infectivity (48-50). How and when EFC polarity is established is
320 unknown. An appealing possibility is that virion tips are stochastically defined by the growth
321 of the palisade long axis during assembly and the EFC and other viral factors polarise at the
322 virion tips after palisade formation by their exclusion from the lateral domains. In such a
323 scenario, palisade formation would drive virion polarity.

324 The EFC mediates fusion of the IMV membrane with the plasma membrane or an endocytic
325 compartment during entry, which releases a naked core into the cytoplasm (51-55).
326 Subsequently, early proteins are produced by early RNA transcripts released from naked
327 cores, which are essential to liberate the DNA genome into the cytosol to initiate replication
328 (1). Our cryo-ET data of naked cores in infected cells indicate the palisade structure does
329 not require surrounding membranes for stability. Furthermore, the loss of lateral bodies
330 from naked cores suggests their association with the palisade depends on the IMV
331 membrane. In addition, we observed flexible 2.6-nm thick polymers fully surrounding naked
332 cores that might correspond to either RNA or the viral genome which is released from the
333 naked core. Finally, we detected ring structures protruding from the palisade surface of
334 naked cores. Analysis of these rings reveals they are compatible in dimension with the
335 hexameric rings of the viral D5 primase/helicase, which is essential for vaccinia genome
336 release (56, 57).
337
338 A common feature of many viral families is the use of a three-dimensional lattice, or capsid,
339 which determines the structure and dimensions of the virion. What distinguishes vaccinia
340 from other viruses is that an initial lattice, D13, is replaced by a second lattice, the palisade,
341 during virion assembly. This contrasts African Swine Fever virus (ASFV), which retains its
342 D13-like lattice, in addition to an inner capsid in mature virions (58). Based on the structural
343 similarities between D13 and the structural components of other viruses with a pseudo-
344 hexameric structure formed by a trimeric protein containing concatenated beta-barrels,
345 vaccinia has been included in the PRD1/adenovirus lineage (59). However, the viral proteins
346 that form the palisade, which is present in the mature particles, may be just as important
347 as D13 in structural phylogenetic comparisons.
348
349 The palisade is a regular capsid-like structure determining the morphology of all forms of
350 vaccinia virions (IMV, IEV, EEV and CEV). The additional membranes acquired by
351 envelopment are different to the IMV viral membrane as they are not corrugated or always
352 in close contact with the IMV surface. Moreover, the acquisition of these membranes is not
353 associated with major changes in the virion structure or palisade architecture (Figure 5).
354 This suggests that these additional membranes are used to facilitate viral egress before cell
355 lysis. In fact, these membranes and associated proteins drive IEV transport on microtubules
356 to the cell periphery, IEV fusion with the plasma membrane and subsequent actin-based
357 transport of CEV (7-11, 13). In contrast, the IMV membrane serves to contain the viral core
358 and lateral bodies and organises the essential components required for entry and, also,
359 envelopment during viral morphogenesis. Based on the strong protein conservation between

360 orthopoxviruses, we believe that the virion assembly of monkeypox and variola major are
361 likely to be identical to that of vaccinia virus we have described here.
362
363 **Methods**
364 **Recombinant viruses**
365 To facilitate cryo-electron microscopy (EM) observations, we produced recombinant
366 Western Reserve (WR) vaccinia strains lacking F11 as this prevents infected cells from
367 rounding-up early during infection (60). In addition, the A36-YdF mutation was used to
368 abolish actin tail formation beneath CEV (11, 13, 61). The F11 gene was deleted in A36 YdF
369 (8) or A36 YdF ΔNPF1-3 (62) backgrounds using the same targeting strategy as previously
370 described (63). Fluorescence was used as a selectable marker to isolate recombinant ΔF11-
371 mCherry viruses by successive rounds of plaque purification in BS-C-1 cells. Correct gene
372 replacement and complete isolation of the recombinant viral strains was confirmed by PCR,
373 sequencing of the F11 locus and western blot analysis.
374
375 **Cell growth, vaccinia infection and vitrification**
376 HeLa cells were maintained in complete MEM (supplemented with 10% Fetal Bovine Serum,
377 100 ug/ml streptomycin and 100 U/ml penicillin) at 37 °C with 5% CO_2. Cells were washed
378 with PBS, treated with trypsin, seeded on glow discharged (40 sec at 45 mA) Quantifoil
379 R3.5/1 gold grids of 200 mesh and placed in wells of 6-well plates with complete MEM. After
380 overnight growth, the cells were infected with A36 YdF ΔF11 or A36 YdF ΔNPF1-3 ΔF11
381 vaccinia virus strains in serum-free MEM at a multiplicity of infection of 2. After one hour,
382 the medium was replaced with complete MEM. At 8 hours post infection the grids were
383 washed once with PBS and excess PBS was removed with a Whatman paper before blotting
384 and vitrification using the Vitrobot Mark IV System, which was set to 95% relative humidity
385 at 22 °C. Colloidal gold particles (10-nm diameter) were pipetted onto grids before blotting,
386 which was performed for 14 s with a relative force of -10.
387
388 **Cryo-electron tomography, image processing and analyses**
389 Grids were first screened on a Talos Arctica TEM (Thermo Fisher) to select edges of cells
390 with an abundance of viral particles that were thin enough for cryo-ET. The precise location
391 of the selected regions on each grid was registered. The grids were subsequently transferred
392 to a Titan Krios (Thermo Fisher) and the mapped grid selections were re-imaged. The Titan
393 Krios was fitted with a K2 Summit direct detector (Gatan) operated in electron counting
394 mode. A Gatan GIF energy filter was used in zero-loss mode with a 20 eV slit width. Dose-
395 symmetric tilt series were collected from -57° to +57° at a 3° increment, a pixel size of

396 4.31 Å and a defocus of -8 µm using Tomography 5.7 software (Thermo Fisher) (Table S2).
397 Four movie frames were collected per tilt with a dose of 1.7 e / Å^2 per tilt, giving a
398 cumulative dose of 66.3 e / Å^2 per tilt series. Movie frames were aligned using alignframes
399 from IMOD (64). Tilt series were aligned using 10-nm Au fiducials or patch tracking in IMOD.
400 Contrast transfer function (CTF) correction and tomogram reconstruction were also
401 implemented in IMOD (64, 65). Alternatively, tomograms were CTF corrected and
402 reconstructed using novaCTF (66). In both cases, a SIRT-like filter equivalent to 5 iterations
403 was routinely applied. Tomogram segmentations were manually performed using AMIRA
404 (Thermo Fisher), mainly using tomograms that were further denoised using ISONet with CTF
405 deconvolution and missing-wedge filling from deep learning (67).
406
407 The diameter of IV, the axes of IMV and their perimeters, and the major axes of IEV and EEV
408 were measured in 3dmod from IMOD using a middle plane of each viral particle. For
409 perimeters, the viral membranes were manually traced to measure their total contour
410 length. As reported previously (23), virions with their dumbbell side view perpendicular to
411 the electron beam were much less frequent than other views. Because of this, for the
412 calculation of the minor axis of IMV we measured the minor axis of both IMV and IMV inside
413 EEV. This is also the reason why we did not find enough side views of IEV to directly measure
414 their minor axis (Table S1). To estimate the IEV minor axis, we measured the thickness that
415 the additional IEV membranes add, and combined it to the calculated IMV minor axis. For
416 volumes calculation, we assumed IV are perfectly spherical and IMV, IEV and EEV triaxial
417 elipsoids.
418
419 **Subtomogram averaging**
420 Tomograms containing IV or IMV were selected for subtomogram averaging (STA). D13 and
421 palisade particles in immature and mature virions respectively were picked from the bin4
422 SIRT-filtered tomograms using oversampled surface models in Dynamo (68), then imported
423 to Relion 3.1 (69) for subsequent subtomogram averaging. Unless otherwise specified, local
424 angular searches about the initial orientations generated in Dynamo were used throughout
425 data processing. For particle extraction, only unbinned weighted back projections
426 reconstructions from novaCTF were used. Lattice measurements were carried out in real
427 space using ChimeraX (70). D13 particles were extracted in 96-pixel boxes at the bin2 pixel
428 size of 4.31Å/pixel. An initial reference was generated using reference-free 3D classification
429 without applied symmetry, with the resulting map clearly showing the honeycomb lattice
430 of D13 trimers. Initial classification and refinement was carried out in both C1 and C6
431 symmetries to verify the symmetry of the D13 hexamer-of-trimers. After initial

classifications and removing of overlapping particles with a distance cutoff of 50Å, particles were re-extracted without binning (4.31Å/pixel) in 192 pixel boxes. Final refinement in C6 symmetry reached 19Å resolution according to the FSC=0.143 criterion.

Palisade particles were initially extracted at binning level 2 (8.62Å/pixel) in 96-pixel boxes. Initial references were generated using independent reference-free 3D classifications for each virion type. This clearly showed the palisade lattice in every case, and the particles for each virion type were from then on processed independently, but in an identical manner. For each virion type, alternating rounds of 3D classification and refinement were used to centre the palisade particles at 2-fold binning. After convergence at 2-fold binning, particles were re-extracted without binning (4.31Å/pixel) in 128-pixel boxes. Overlapping particles were removed with a distance cutoff of 40Å before further refinements were carried out without binning. As all refinements converged on maps with identical lattices, particles from all virion types except for the naked cores were then combined for further refinements. All refinements were carried out without application of symmetry up to this point. After the C1 maps converged and the symmetry of the lattice was apparent, further refinement runs were carried out with C3 symmetry applied. The final resolutions of the palisade maps ranged from 20-30Å, according to the FSC=0.143 criterion.

Immunofluorescence imaging

HeLa cells were plated on fibronectin-coated coverslips and infected with an RFP-A3 vaccinia strain (71) for 8 hours and fixed with 4% paraformaldehyde in PBS for 10 min, then permeabilised with 0.1% Triton X-100 in PBS for 5 min and incubated in blocking buffer (10 mM MES pH 6.1, 150 mM NaCl, 5 mM EGTA, 5 mM $MgCl_2$, and 5 mM glucose) containing 2% (v/v) fetal calf serum and 1% (w/v) BSA for 30 min prior to addition of 4′,6-diamidino-2-phenylindole (DAPI) for 5 minutes, before mounting the coverslips using Mowiol. Coverslips were imaged on an Olympus iX83 Microscope with Olympus 150x/1.45 NA X-Line Apochromatic Objective Lens, dual Photometrics BSI-Express sCMOS cameras and CoolLED pE-300 Light Source (Visitech) and was controlled using Micro-Manager 2.0.0. Image stacks of 10-15 z-slices with 0.1 µm steps were acquired and deconvolved using the express deconvolution setting on Huygens Software (Scientific Volume Imaging).

Acknowledgements

We thank Alessandro Costa, Neil McDonald and Jeremy Carlton (Francis Crick Institute) as well as the Way lab for insightful comments on the manuscript as well as LuYan Cao for providing the initial slide of infected cells used in our SIM analysis (Fig. 2F). We also

468 acknowledge Philip Walker and Andy Purkiss of the Structural Biology Science Technology
469 Platform and the Scientific Computing Science Technology Platform for computational
470 support. MHG also thanks Pauline McIntosh (Francis Crick Institute) for guidance during the
471 initial stages of the project. The work in the Way and Rosenthal labs was supported by the
472 Francis Crick Institute, which receives its core funding from Cancer Research UK (FC001209
473 and FC001143), the UK Medical Research Council (FC001209 and FC001143), and the
474 Wellcome Trust (FC001209 and FC001143). The funders had no role in study design, data
475 collection and analysis, decision to publish, or preparation of the manuscript. For the
476 purpose of Open Access, the authors have applied a CC BY public copyright license to any
477 Author Accepted Manuscript version arising from this submission.
478

479 **Author contributions**

480 All authors designed the research program and strategy. MHG, TC and AN performed
481 research, MHG and TC analyzed data and MHG, TC, PBR and MW wrote the paper.
482

483 **Competing interests**

484 The authors have no competing financial interests
485

486 **References**

487 1. B. Moss, "Poxviridae: the viruses and their replication" in Fields Virology, H. P. Knipe
488 DM, Ed. (Lippincott Williams and Wilkins, Philadelphia, 2007), pp. 2905-2946.

489 2. B. L. Jacobs *et al.*, Vaccinia virus vaccines: past, present and future. *Antiviral Res*
490 **84**, 1-13 (2009).

491 3. S. R. Walsh, R. Dolin, Vaccinia viruses: vaccines against smallpox and vectors against
492 infectious diseases and tumors. *Expert Rev Vaccines* **10**, 1221-1240 (2011).

493 4. K. L. Roberts, G. L. Smith, Vaccinia virus morphogenesis and dissemination. *Trends*
494 *Microbiol* **16**, 472-479 (2008).

495 5. M. Schmelz *et al.*, Assembly of vaccinia virus: the second wrapping cisterna is derived
496 from the trans Golgi network. *J Virol* **68**, 130-147 (1994).

497 6. J. Tooze, M. Hollinshead, B. Reis, K. Radsak, H. Kern, Progeny vaccinia and human
498 cytomegalovirus particles utilize early endosomal cisternae for their envelopes. *Eur J Cell*
499 *Biol* **60**, 163-178 (1993).

500 7. G. L. Smith, A. Vanderplasschen, M. Law, The formation and function of extracellular
501 enveloped vaccinia virus. *J Gen Virol* **83**, 2915-2931 (2002).

502 8. J. Rietdorf *et al.*, Kinesin-dependent movement on microtubules precedes actin-
503 based motility of vaccinia virus. *Nat Cell Biol* **3**, 992-1000 (2001).

504 9. F. Leite, M. Way, The role of signalling and the cytoskeleton during Vaccinia Virus
505 egress. *Virus Res* **209**, 87-99 (2015).

506 10. S. Cudmore, P. Cossart, G. Griffiths, M. Way, Actin-based motility of vaccinia virus.
507 *Nature* **378**, 636-638 (1995).

508 11. F. Frischknecht *et al.*, Actin-based motility of vaccinia virus mimics receptor tyrosine
509 kinase signalling. *Nature* **401**, 926-929 (1999).

510 12. M. Hollinshead *et al.*, Vaccinia virus utilizes microtubules for movement to the cell
511 surface. *J Cell Biol* **154**, 389-402 (2001).

512 13. B. M. Ward, B. Moss, Vaccinia virus intracellular movement is associated with
513 microtubules and independent of actin tails. *J Virol* **75**, 11651-11663 (2001).

514 14. A. S. Weisberg *et al.*, Enigmatic origin of the poxvirus membrane from the
515 endoplasmic reticulum shown by 3D imaging of vaccinia virus assembly mutants. *Proc Natl*
516 *Acad Sci U S A* **114**, E11001-E11009 (2017).

517 15. B. Moss, Poxvirus membrane biogenesis. *Virology* **479-480**, 619-626 (2015).

518 16. P. Chlanda, M. A. Carbajal, M. Cyrklaff, G. Griffiths, J. Krijnse-Locker, Membrane
519 rupture generates single open membrane sheets during vaccinia virus assembly. *Cell Host*
520 *Microbe* **6**, 81-90 (2009).

521 17. J. Heuser, Deep-etch EM reveals that the early poxvirus envelope is a single
522 membrane bilayer stabilized by a geodetic "honeycomb" surface coat. *J Cell Biol* **169**, 269-
523 283 (2005).

524 18. P. Szajner, A. S. Weisberg, J. Lebowitz, J. Heuser, B. Moss, External scaffold of
525 spherical immature poxvirus particles is made of protein trimers, forming a honeycomb
526 lattice. *J Cell Biol* **170**, 971-981 (2005).

527 19. J. Hyun, H. Matsunami, T. G. Kim, M. Wolf, Assembly mechanism of the pleomorphic
528 immature poxvirus scaffold. *Nat Commun* **13**, 1704 (2022).

529 20. M. W. Bahar, S. C. Graham, D. I. Stuart, J. M. Grimes, Insights into the evolution of
530 a complex virus from the crystal structure of vaccinia virus D13. *Structure* **19**, 1011-1020
531 (2011).

532 21. D. Garriga *et al.*, Structural basis for the inhibition of poxvirus assembly by the
533 antibiotic rifampicin. *Proc Natl Acad Sci U S A* **115**, 8424-8429 (2018).

534 22. J. K. Hyun *et al.*, Membrane remodeling by the double-barrel scaffolding protein of
535 poxvirus. *PLoS Pathog* **7**, e1002239 (2011).

536 23. R. C. Condit, N. Moussatche, P. Traktman, In a nutshell: structure and assembly of
537 the vaccinia virion. *Adv Virus Res* **66**, 31-124 (2006).

538 24. C. Ansarah-Sobrinho, B. Moss, Role of the I7 protein in proteolytic processing of
539 vaccinia virus membrane and core components. *J Virol* **78**, 6335-6343 (2004).

540 25. T. G. Senkevich, C. L. White, E. V. Koonin, B. Moss, Complete pathway for protein
541 disulfide bond formation encoded by poxviruses. *Proc Natl Acad Sci U S A* **99**, 6667-6672
542 (2002).

543 26. M. Cyrklaff *et al.*, Cryo-electron tomography of vaccinia virus. *Proc Natl Acad Sci U*
544 *S A* **102**, 2772-2777 (2005).

545 27. J. Dubochet, M. Adrian, K. Richter, J. Garces, R. Wittek, Structure of intracellular
546 mature vaccinia virus observed by cryoelectron microscopy. *J Virol* **68**, 1935-1941 (1994).

547 28. G. Griffiths, N. Roos, S. Schleich, J. K. Locker, Structure and assembly of
548 intracellular mature vaccinia virus: thin-section analyses. *J Virol* **75**, 11056-11070 (2001).

549 29. A. R. Mohandas, S. Dales, Involvement of spicules in the formation of vaccinia virus
550 envelopes elucidated by a conditional lethal mutant. *Virology* **214**, 494-502 (1995).

551 30. C. Morgan, The insertion of DNA into vaccinia virus. *Science* **193**, 591-592 (1976).

552 31. N. Roos *et al.*, A novel immunogold cryoelectron microscopic approach to investigate
553 the structure of the intracellular and extracellular forms of vaccinia virus. *EMBO J* **15**, 2343-
554 2355 (1996).

555 32. M. Cyrklaff *et al.*, Whole cell cryo-electron tomography reveals distinct disassembly
556 intermediates of vaccinia virus. *PLoS One* **2**, e420 (2007).

557 33. B. Unger, J. Mercer, K. A. Boyle, P. Traktman, Biogenesis of the vaccinia virus
558 membrane: genetic and ultrastructural analysis of the contributions of the A14 and A17
559 proteins. *J Virol* **87**, 1083-1097 (2013).

560 34. H. Bisht, A. S. Weisberg, P. Szajner, B. Moss, Assembly and disassembly of the capsid-
561 like external scaffold of immature virions during vaccinia virus morphogenesis. *J Virol* **83**,
562 9140-9150 (2009).

563 35. M. Faini, R. Beck, F. T. Wieland, J. A. Briggs, Vesicle coats: structure, function, and
564 general principles of assembly. *Trends Cell Biol* **23**, 279-288 (2013).

565 36. T. Kirchhausen, Three ways to make a vesicle. *Nat Rev Mol Cell Biol* **1**, 187-198
566 (2000).

567 37. J. C. Stachowiak, F. M. Brodsky, E. A. Miller, A cost-benefit analysis of the physical
568 mechanisms of membrane curvature. *Nat Cell Biol* **15**, 1019-1027 (2013).

569 38. J. C. Stachowiak *et al.*, Membrane bending by protein-protein crowding. *Nat Cell*
570 *Biol* **14**, 944-949 (2012).

571 39. K. J. Erlandson *et al.*, Poxviruses Encode a Reticulon-Like Protein that Promotes
572 Membrane Curvature. *Cell Rep* **14**, 2084-2091 (2016).

573 40. B. Sodeik *et al.*, Assembly of vaccinia virus: role of the intermediate compartment
574 between the endoplasmic reticulum and the Golgi stacks. *J Cell Biol* **121**, 521-541 (1993).

575 41. J. R. Rodriguez, C. Risco, J. L. Carrascosa, M. Esteban, D. Rodriguez, Vaccinia virus
576 15-kilodalton (A14L) protein is essential for assembly and attachment of viral crescents to
577 virosomes. *J Virol* **72**, 1287-1296 (1998).

578 42. M. Ericsson *et al.*, Characterization of ts 16, a temperature-sensitive mutant of
579 vaccinia virus. *J Virol* **69**, 7072-7086 (1995).

580 43. W. W. Yeh, B. Moss, E. J. Wolffe, The vaccinia virus A9L gene encodes a membrane
581 protein required for an early step in virion morphogenesis. *J Virol* **74**, 9701-9711 (2000).

582 44. S. Cudmore *et al.*, A vaccinia virus core protein, p39, is membrane associated. *J*
583 *Virol* **70**, 6909-6921 (1996).

584 45. S. Wilton, A. R. Mohandas, S. Dales, Organization of the vaccinia envelope and
585 relationship to the structure of intracellular mature virions. *Virology* **214**, 503-511 (1995).

586 46. J. A. Briggs *et al.*, The mechanism of HIV-1 core assembly: insights from three-
587 dimensional reconstructions of authentic virions. *Structure* **14**, 15-20 (2006).

588 47. J. A. Briggs, T. Wilk, R. Welker, H. G. Krausslich, S. D. Fuller, Structural organization
589 of authentic, mature HIV-1 virions and cores. *EMBO J* **22**, 1707-1715 (2003).

590 48. R. D. M. Gray *et al.*, Nanoscale polarization of the entry fusion complex of vaccinia
591 virus drives efficient fusion. *Nat Microbiol* **4**, 1636-1644 (2019).

592 49. T. G. Senkevich, B. M. Ward, B. Moss, Vaccinia virus entry into cells is dependent on
593 a virion surface protein encoded by the A28L gene. *J Virol* **78**, 2357-2366 (2004).

594 50. B. Moss, Poxvirus cell entry: how many proteins does it take? *Viruses* **4**, 688-707
595 (2012).

596 51. F. I. Schmidt, C. K. Bleck, A. Helenius, J. Mercer, Vaccinia extracellular virions enter
597 cells by macropinocytosis and acid-activated membrane rupture. *EMBO J* **30**, 3647-3661
598 (2011).

599 52. J. Mercer, A. Helenius, Vaccinia virus uses macropinocytosis and apoptotic mimicry
600 to enter host cells. *Science* **320**, 531-535 (2008).

601 53. R. A. Janeczko, J. F. Rodriguez, M. Esteban, Studies on the mechanism of entry of
602 vaccinia virus in animal cells. *Arch Virol* **92**, 135-150 (1987).

603 54. G. C. Carter, M. Law, M. Hollinshead, G. L. Smith, Entry of the vaccinia virus
604 intracellular mature virion and its interactions with glycosaminoglycans. *J Gen Virol* **86**,
605 1279-1290 (2005).

606 55. R. W. Doms, R. Blumenthal, B. Moss, Fusion of intra- and extracellular forms of
607 vaccinia virus with the cell membrane. *J Virol* **64**, 4884-4892 (1990).

608 56. S. Kilcher *et al.*, siRNA screen of early poxvirus genes identifies the AAA+ ATPase D5
609 as the virus genome-uncoating factor. *Cell Host Microbe* **15**, 103-112 (2014).

610 57. S. Hutin *et al.*, Domain Organization of Vaccinia Virus Helicase-Primase D5. *J Virol*
611 **90**, 4604-4613 (2016).

612 58. N. Wang *et al.*, Architecture of African swine fever virus and implications for viral
613 assembly. *Science* **366**, 640-644 (2019).

614 59. N. G. Abrescia, D. H. Bamford, J. M. Grimes, D. I. Stuart, Structure unifies the viral
615 universe. *Annu Rev Biochem* **81**, 795-822 (2012).

616 60. C. H. Durkin *et al.*, RhoD Inhibits RhoC-ROCK-Dependent Cell Contraction via PAK6.
617 *Dev Cell* **41**, 315-329 e317 (2017).

618 61. H. Lynn *et al.*, Loss of cytoskeletal transport during egress critically attenuates
619 ectromelia virus infection in vivo. *J Virol* **86**, 7427-7443 (2012).

620 62. X. Snetkov, I. Weisswange, J. Pfanzelter, A. C. Humphries, M. Way, NPF motifs in
621 the vaccinia virus protein A36 recruit intersectin-1 to promote Cdc42:N-WASP-mediated
622 viral release from infected cells. *Nat Microbiol* **1**, 16141 (2016).

623 63. J. V. Cordeiro *et al.*, F11-mediated inhibition of RhoA signalling enhances the spread
624 of vaccinia virus in vitro and in vivo in an intranasal mouse model of infection. *PLoS One* **4**,
625 e8506 (2009).

626 64. J. R. Kremer, D. N. Mastronarde, J. R. McIntosh, Computer visualization of three-
627 dimensional image data using IMOD. *J Struct Biol* **116**, 71-76 (1996).

628 65. Q. Xiong, M. K. Morphew, C. L. Schwartz, A. H. Hoenger, D. N. Mastronarde, CTF
629 determination and correction for low dose tomographic tilt series. *J Struct Biol* **168**, 378-
630 387 (2009).

631 66. B. Turonova, F. K. M. Schur, W. Wan, J. A. G. Briggs, Efficient 3D-CTF correction for
632 cryo-electron tomography using NovaCTF improves subtomogram averaging resolution to
633 3.4A. *J Struct Biol* **199**, 187-195 (2017).

634 67. Y.-T. Liu *et al.*, Isotropic Reconstruction of Electron Tomograms with Deep Learning.
635 *bioRxiv* 10.1101/2021.07.17.452128, 2021.2007.2017.452128 (2021).

636 68. D. Castano-Diez, M. Kudryashev, H. Stahlberg, Dynamo Catalogue: Geometrical tools
637 and data management for particle picking in subtomogram averaging of cryo-electron
638 tomograms. *J Struct Biol* **197**, 135-144 (2017).

639 69. T. A. M. Bharat, C. J. Russo, J. Lowe, L. A. Passmore, S. H. W. Scheres, Advances in
640 Single-Particle Electron Cryomicroscopy Structure Determination applied to Sub-tomogram
641 Averaging. *Structure* **23**, 1743-1753 (2015).

642 70. E. F. Pettersen *et al.*, UCSF ChimeraX: Structure visualization for researchers,
643 educators, and developers. *Protein Sci* **30**, 70-82 (2021).

644 71. I. Weisswange, T. P. Newsome, S. Schleich, M. Way, The rate of N-WASP exchange
645 limits the extent of ARP2/3-complex-dependent actin-based motility. *Nature* **458**, 87-91
646 (2009).
647

648 **Legends**

649 **Figure 1. Cryo-ET of vaccinia infected cells.**

650 **A**. Schematic representation of the different stages in vaccinia assembly and envelopment.
651 D13 coated membrane crescents initially close to form a spherical IV, that mature into brick
652 shaped IMV with dumbbell shaped viral core flanked by two lateral bodies (red).
653 Envelopment of IMV by a Golgi membrane cisterna or endosomal compartment (green)
654 results in the formation of triple membraned IEV, which can fuse with the plasma membrane
655 to liberate extracellular enveloped virions (EEV), which are called CEV if they remain
656 attached to the surface of the cell. **B.** Left: Central section of a tomogram showing fully
657 formed IV. The red arrow points at an IV with a lateral invagination. Invaginations in other
658 IV can be seen in the 3D-segmented model of the membrane of the same tomogram (right)
659 (See Movie 1). **C.** Tomogram middle view (left) and its corresponding segmentation (right)
660 of IMV (See Movie 2). A "cut corner" (magenta arrows) is apparent in some IMV. Scalebars =
661 100 nm.
662

663 **Figure 2. The stages of IV assembly**

664 **A.** Tomogram section showing D13 coated membrane crescents with open ends (indicated
665 magenta arrowheads). **B.** Tomogram sections showing the last stages of IV membrane
666 closure: the middle view (left) reveals membrane discontinuity (indicated magenta
667 arrowheads) while in the higher plane at + 48 nm relative to the middle view (right) the
668 membrane is continuous (see Movie 3). **C.** Closed IV containing a condensed nucleoid
669 (outlined in magenta) with repeated structural features (magenta arrowheads). **D.**
670 Cytoplasmic condensed nucleoid/s next to an IV. **E.** Extended nucleoid/s in association with
671 an open IV. **F.** Structured illumination microscopy image of infected cell showing condensed
672 DNA structures (green) in association with RFP-A3 positive viral particles (magenta) located
673 in a perinuclear viral factory. Tomogram Scalebars = 100 nm.

674 **Figure 3. In situ structure of the D13 lattice.**
675 **A.** Tomogram section as indicated in the schematic on the left through the middle and top
676 of a representative IV (see Movie 4). The densities corresponding to the D13 lattice are
677 coloured in magenta in panels (right) and show pseudo-hexagonal organisation. Scale bar =
678 100 nm. **B.** Map based on subtomogram averaging of D13 and the underlying IV membrane
679 from a top (left) and a side (right) view with fitting of coordinate models of D13 trimers(PDB
680 7VFE) shown in blue/brown.
681
682 **Figure 4. Ultrastructure of IMV.**
683 **A.** Central plane of a tomogram showing the broadest view of a representative IMV together
684 with a region magnified 2.5-times to highlight the outer layer, viral membrane, palisade
685 and inner wall of the virion (see Movie 5). **B.** Lateral view of an IMV, showing the lateral
686 bodies (outlined in red) and the dumbbell shape of the core. The magnified regions outlined
687 in magenta show the same characteristic IMV layers. **C.** Different sections of the IMV shown
688 in A at the indicated plane positions in nm. The insert in the +31 nm view shows the surface
689 of the palisade lattice. In the second row, yellow highlights the palisade structure, while
690 red indicates the lateral body in the +52 nm view. **D.** The first row shows a schematic
691 representation of the views displayed in C, while the second row represents the orthogonal
692 view together with the tomogram position (black line). **E.** Left: Top and side views of a
693 segmentation model of the IMV in A. The outer layer (blue) and viral membrane (black) are
694 cut away so the internal palisade (yellow) and the lateral bodies (red) can be seen (see
695 Movie 6). Right: The dumbbell shaped core is more apparent in a Simulated Digitally
696 Reconstructed Radiograph (DDR Rendering) of the same segmentation model. Scale bars =
697 100 nm.
698
699 **Figure 5. Ultrastructure of the naked viral core.**
700 **A.** Middle section of a tomogram showing a naked viral core together with a region
701 magnified 3 times to highlight the palisade and inner wall as well as the polymers that
702 surround the core. **B.** A higher tomogram section (+ 41 nm) of the same naked viral core
703 highlighting the pseudohexagonal lattice of the palisade. **C.** At an even higher section (+58
704 nm) ring structures associated with the palisade are evident. The dimensions of the rings
705 (n=25) from 5 naked cores are indicated together with the standard error of the mean. Scale
706 bars = 100 nm.
707
708
709

710 **Figure 6. The palisade is a pseudohexagonal lattice composed of trimeric proteins.**
711 **A.** Central plane of a tomograms showing that the additional membranes of IEV and CEV
712 (associated with the plasma membrane, PM) do not alter the ultrastructure of the internal
713 IMV. Scale bar = 100 nm. **B.** Schematic representation to illustrate the number of membranes
714 of IMV, IEV and EEV/CEV. **C.** Sections through the palisade layer corresponding to the virions
715 shown in A. Scale bar = 10 nm. **D.** Map derived from subtomogram averaging showing the
716 inner wall, palisade layer, viral membrane, and outer layer in surface representation (left)
717 and corresponding sections of the map (right).
718
719 **Figure 7. Maturation of vaccinia virus: from IV to IMV.**
720 **A.** Table showing the measured dimensions of middle views of IV (diameter, n = 26;
721 perimeter, n = 15) and IMV (major axis, n = 22; intermediate axis, n = 19; minor axis, n =
722 10; perimeter, n = 19) tomograms. * indicates that the IMV minor axis was calculated from
723 the side views of 3 IMV and 7 IMV inside EEV (see methods for explanation). For volume
724 calculation IV and IMV were assumed to be spheres and triaxial ellipsoids respectively. **B.**
725 Plots showing the individual values for perimeter and diameter / major axis (indicated by
726 magenta lines in schematics below graph) of the IV, IMV and EEV. IV and IMV measurements
727 were used to calculate the averages shown in A. The averages of the EEV inner most
728 membrane perimeter and major axis are 1074.46 nm ± 7.09 nm and 348.91 ± 1.87 nm,
729 respectively. **C.** Central sections of IV and IMV along with possible intermediates together
730 with magnified regions (2.5-times) highlighting the different layers of each particle. Scale
731 bar = 100 nm. **D.** Vaccinia maturation model: the palisade lattice (yellow) forms inside D13-
732 coated IV, its maximum length being determined by the IV diameter. Following disassembly
733 of the D13 lattice, the viral membrane acquires the shape of the palisade and becomes
734 wrinkled. During this process, the presence of two lateral bodies (red) results in the
735 deformation of the core so it adopts its characteristic biconcave shape.
736
737 **Supplementary Table 1. Measurements and calculations of virion dimensions.**
738 **A.** The middle-view perimeters, IV diameter, the major axis of IMV and EEV/CEV are shown,
739 together with the standard error of the mean (SEM) and the number of viral particles
740 measured. The intermediate and minor axes of IMV are also shown, as well as the IEV axes.
741 Finally, the calculated volume of IV, IMV and IEV are provided. See Methods for details of
742 dimension calculations. **B**. For the thickness of the inner wall and the outer layer, 5
743 different IMV were measured by tracing 5 different lines for each IMV, which correspond to
744 the five measurements shown. To estimate the distance between the palisade and the viral
745 membrane (with no lateral bodies) 5 IMV were used. For the distance between the palisade

746 and the plasma membrane through lateral bodies 1 IMV and 4 EEV were included in the
747 quantification. All values correspond to nm.
748
749 **Supplementary Table 2. Cryo-ET data collection and STA processing.**
750
751 **Supplementary Figure 1. Low-magnification images of vaccinia infected HeLa cells on**
752 **grids. A**. The pink circle marks the position where the IV in Figure 1B were imaged. The
753 image on the right is a magnification of the circled area and its surroundings. **B**. A cryo-EM
754 image showing IV (magenta arrow) and IMV (green arrow) visualised at low magnification in
755 cells over holes in the carbon support film. Scale bars = 10 (left) and 1 µm (right) (A) and 1
756 µm (B).
757
758 **Supplementary Figure 2. Tomographic gallery of IV with nucleoids**
759 Tomographic sections showing IV with an internal condensed nucleoid outlined in magenta
760 in the bottom row. Scale bar = 100 nm.
761
762 **Supplementary Figure 3. Examples of IMV with cut corners**
763 Gallery of tomographic sections of IMV showing cut or flattened corner/s (black
764 arrowheads). Scale bar = 100 nm.
765
766 **Supplementary Figure 4. Palisade maps from IMV, IEV and EEV/CEV.**
767 **A**. Maps derived from subtomogram averaging IMV, IEV or EEV/CEV. A surface (top) and a
768 cut-section view (bottom) are shown. **B**. Fourier Shell Correlation plots for palisade maps as
769 well as for the D13 map. Curves are given for the corrected, unmasked, masked and masked
770 with phase randomisations calculations.
771
772 **Movie 1. IV overview.**
773 Tomogram of an intracellular region accumulating IV, which corresponds to the section
774 shown in Figure 1B. IV membranes are segmented in red
775
776 **Movie 2. IMV overview**.
777 Tomogram showing IMV in the cytoplasm, which corresponds to the section shown in Figure
778 1C. IMV membrane is segmented in blue, microtubules in red and the lumen of an ER-like
779 compartment in yellow.
780

Movie 3. IV assembly. Tomogram of an IV with a pore on the viral membrane (pore labelled with magenta arrowheads). Sections of this tomograms are shown in Figure 2B.

Movie 4. Ultrastructure of IV.
Tomogram corresponding to the IV shown in Figure 3A. Scale bar = 100 nm.

Movie 5. Ultrastructure of IMV.
Tomogram of the IMV particle shown in Figure 4A. Scale bar = 100 nm.

Movie 6. Segmentation of an IMV. The movie shows the segmentation performed on the IMV from Figure 4A. Blue is the outer layer and black labels the viral membrane, while yellow corresponds to the palisade lattice and red to the lateral bodies.

Movie 7. Ultrastructure of the naked viral core.
Tomogram of the naked core shown in Figure 5. The central magenta square marks part of the palisade, the top magenta rectangle highlights the flexible polymer observed and the small magenta squares at the end of the movie outline the ring-like structures protruding from the palisade. Scale bar = 100 nm.

817 **Supplementary Table 1. Measurements and calculations of virion dimensions.**

818

819 **A.**

Middle view perimeter	Average (nm)	SEM	
IV	1106.39	8.58	n = 15
IMV	1087.75	11.25	n = 19
EEV / CEV	1074.46	7.09	n = 20

820

821

Diameter / major axis	Average (nm)	Standard Error of the Mean (SEM)	
IV	351.89	2.88	n = 26
IMV	351.70	3.31	n = 22
EEV / CEV	348.91	1.87	n = 22

822

823

IMV	Average (nm)	SEM	
Intermediate axis	280.53	3.66	n = 19
Minor axis*	198.04	4.94	n = 10 (3 IMV, 7 EEV)

824

825

IEV	Average (nm)	SEM	
Major axis	437.86	13.88	n = 7
Intermediate axis	383.45112	10.95	n = 7
Minor axis (estimation)	259.11		

826

827

	Calculated volume (nm^3)
IV	2.28×10^7
IMV	1.02×10^7
IEV	2.28×10^7

828

829

830

831

832

833 **B.**

Inner wall thickness (nm)	IMV1	IMV2	IMV3	IMV4	IMV5			
1	4.89	4.12	2.08	4.43	3.72			
2	4.29	3.88	4.28	3.20	2.71			
3	3.54	4.21	4.75	3.11	4.78			
4	3.25	3.48	3.61	2.38	4.28	Final average	Standard Deviation	SEM
5	3.91	4.02	2.81	6.05	4.20			
average	3.98	3.94	3.51	3.84	3.94	3.84	0.19	0.09

834

Outer layer thickness (nm)	IMV1	IMV2	IMV3	IMV4	IMV5			
1	7.24	8.15	6.14	6.90	5.61			
2	7.51	7.14	7.25	6.52	7.31			
3	7.48	6.55	5.86	6.37	5.05			
4	6.40	7.12	6.03	6.96	6.63	Final average	Standard Deviation	SEM
5	5.58	5.77	7.71	6.28	7.11			
average	6.84	6.95	6.60	6.61	6.34	6.67	0.11	0.24

835

Palisade-to-viral membrane distance (nm)	IMV1	IMV3	IMV4	IMV5			
1	9.54	10.12	8.89	9.47			
2	9.57	9.37	7.87	8.08			
3	11.18	9.51	8.32	8.31	Final average	Standard Deviation	SEM
4	8.89	9.57	11.28	10.98			
5	8.66	8.53	7.36	10.04			
average	9.57	9.42	8.74	9.38	9.28	0.18	0.36

836

Palisade to viral membrane through lateral bodies (nm)	IMV1	EEV1	EEV2	EEV3	EEV4	Average	Standard Deviation	SEM
1	53.20	50.35	43.45	52.01	41.76			
2	31.93	48.19	42.39	62.64	39.35	46.53	8.60	2.72

837

838 **Supplementary Table S2. Cryo-ET data collection and STA processing.**

839

	Palisade				D13
	Combined	EEV/CEV	IMV	IEV	
Data collection					
Voltage (kV)	300				
Cumulative electron dose (e / $Å^2$)	66.3				
Applied defocus (µm)	-8				
Pixel size (Å)	4.31				
Tilt range (°)	±57°, dose symmetric				
STA processing					
Map symmetry	C3	C3	C3	C3	C6
Initial particle number	182938	209703	80698	8256	341376
Final particle number	179822	149662	27590	5686	34092
Map resolution (Å) (FSC=0.143)	21.2	21.2	25.1	30.6	19.2

840

841

A

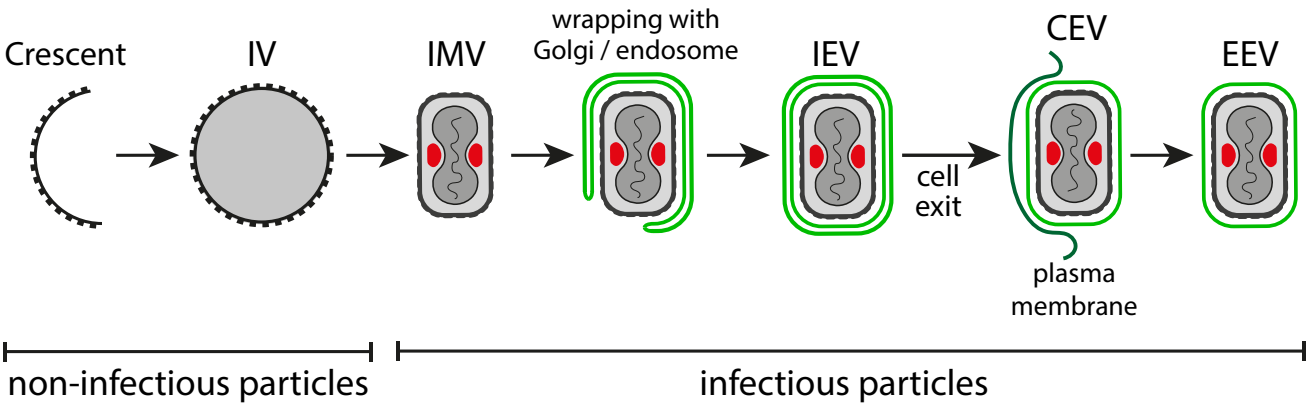
Crescent
IV
IMV
wrapping with
Golgi / endosome
IEV
cell
exit
CEV
plasma
membrane
EEV
non-infectious particles
infectious particles

B

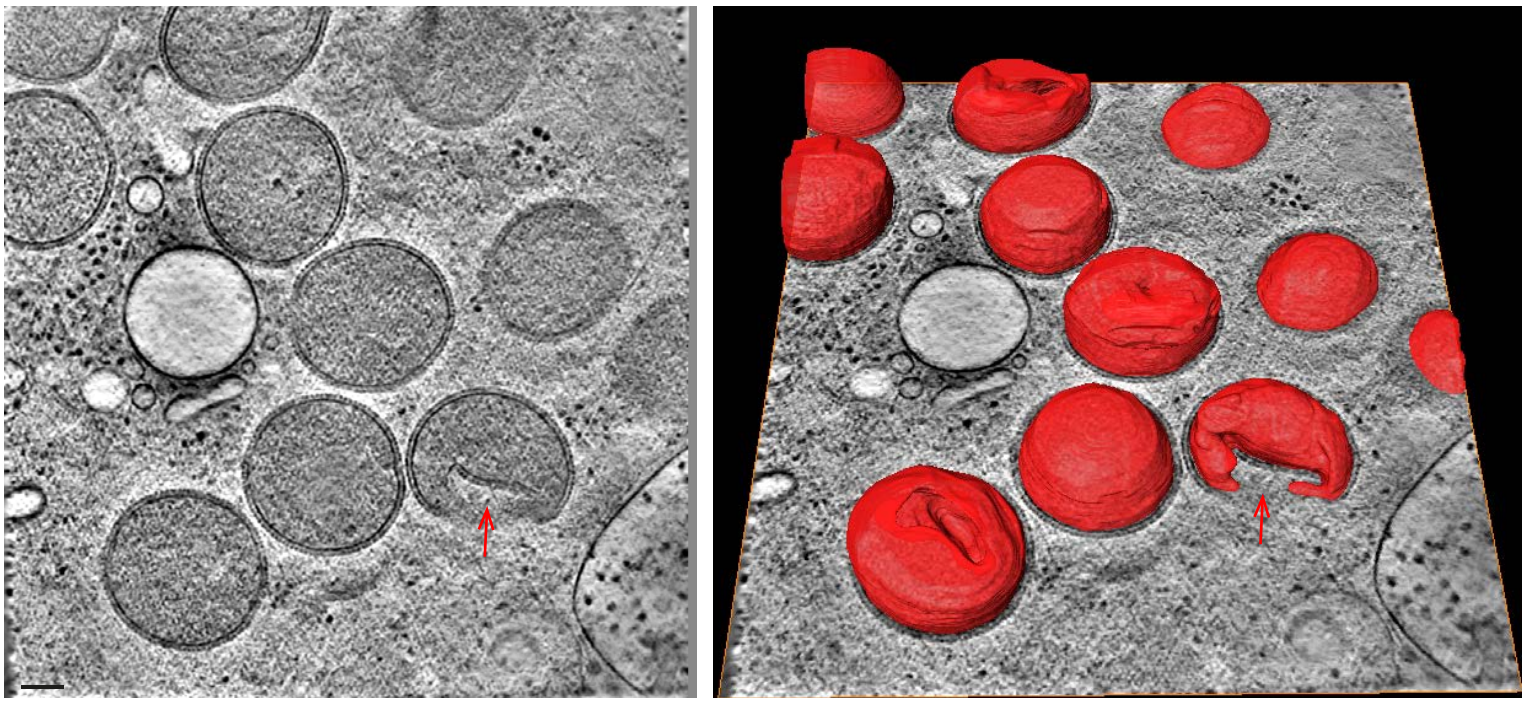

C

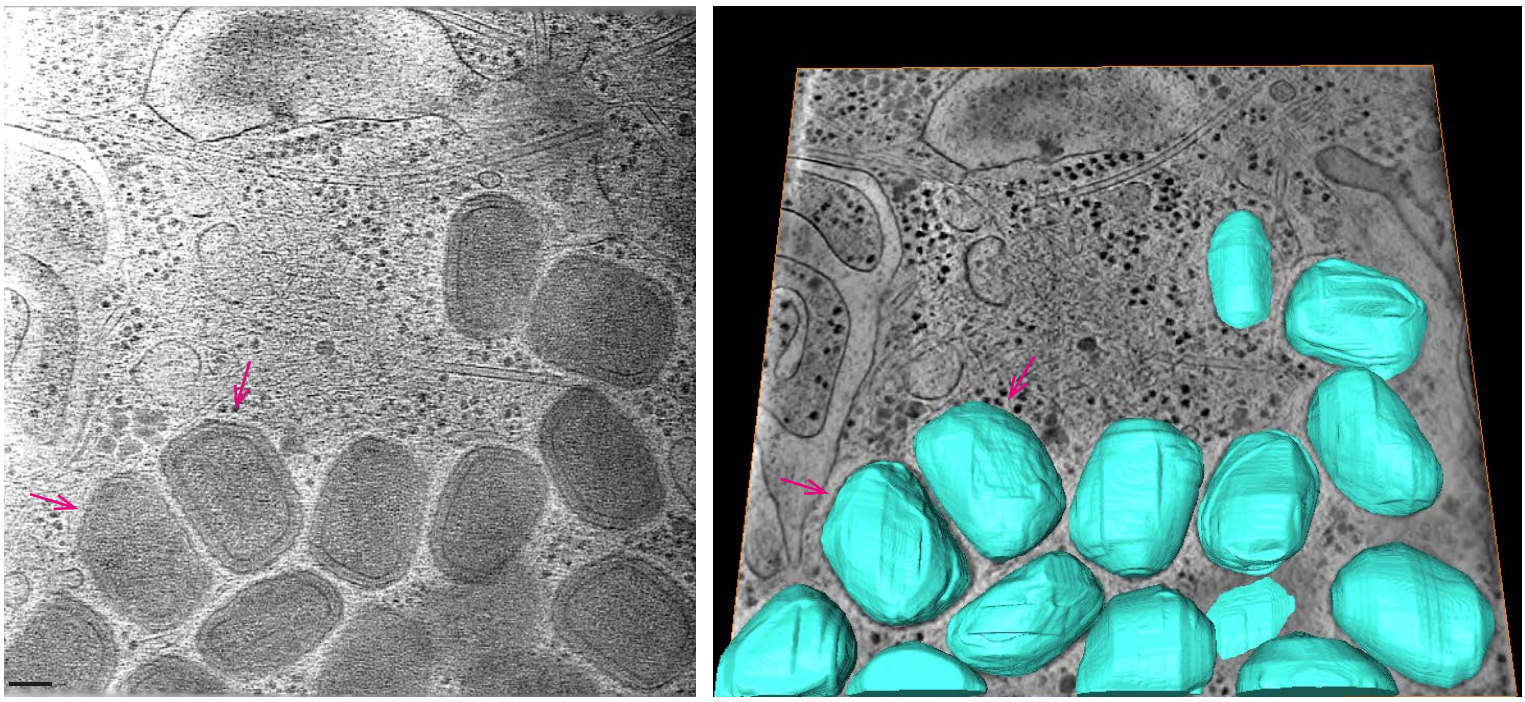

Figure 1

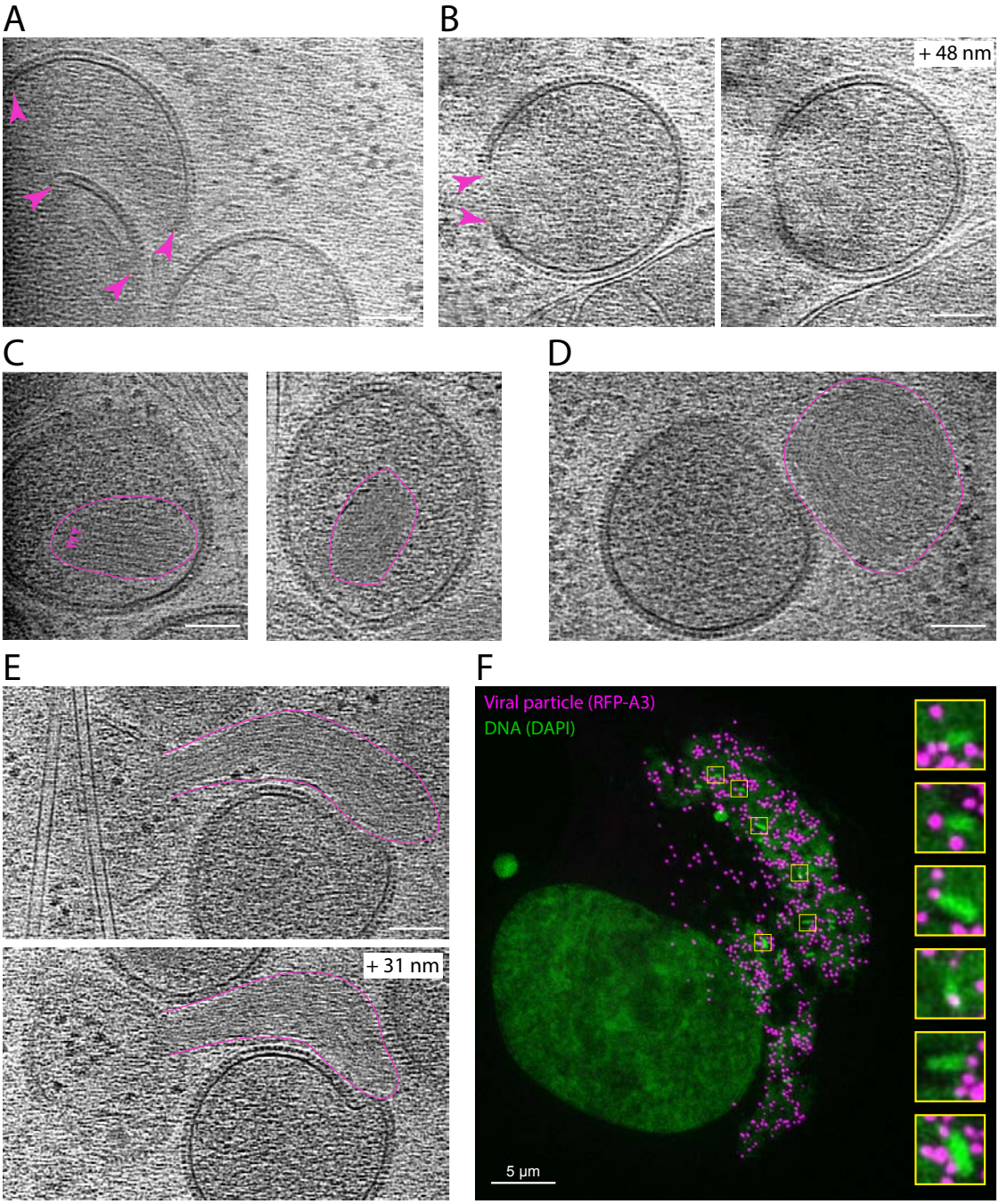

Figure 2

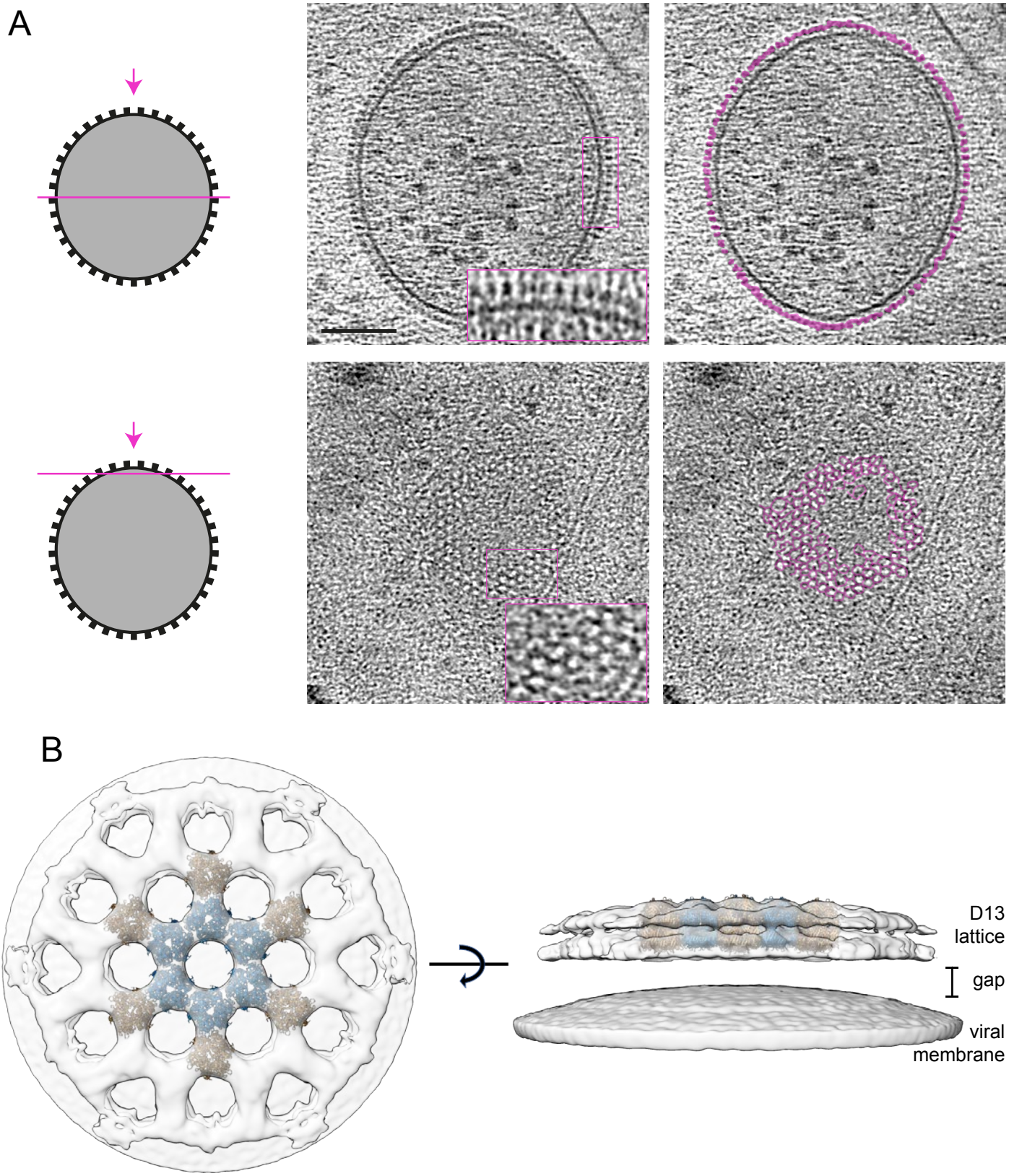

Figure 3

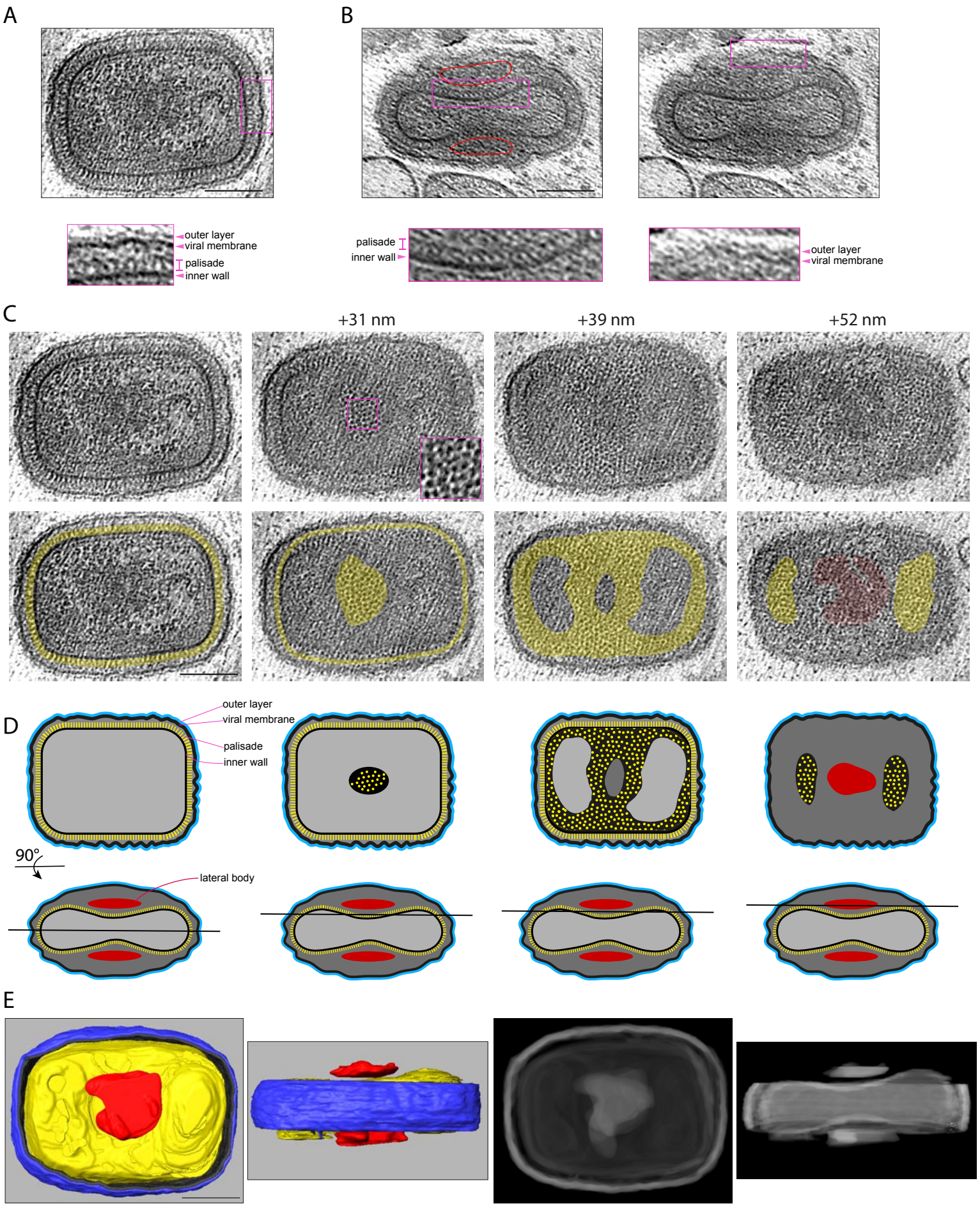
A
B
outer layer
viral membrane
palisade
inner wall
palisade
inner wall
outer layer
viral membrane
C
+31 nm
+39 nm
+52 nm
D
outer layer
viral membrane
palisade
inner wall
90°
lateral body
E

Figure 4

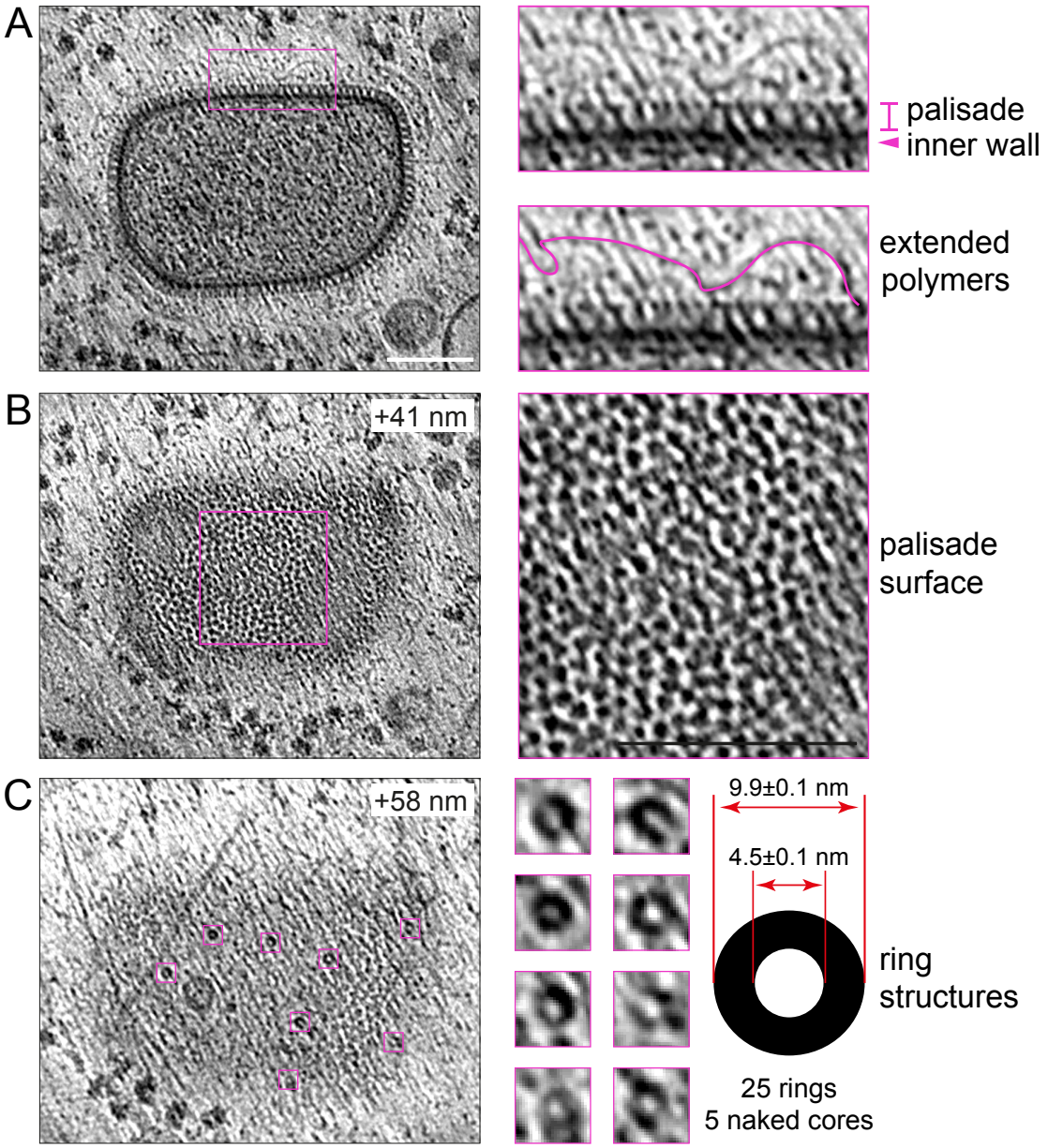
A
palisade
inner wall
extended
polymers
B
+41 nm
palisade
surface
C
+58 nm
9.9±0.1 nm
4.5±0.1 nm
ring
structures
25 rings
5 naked cores

Figure 5

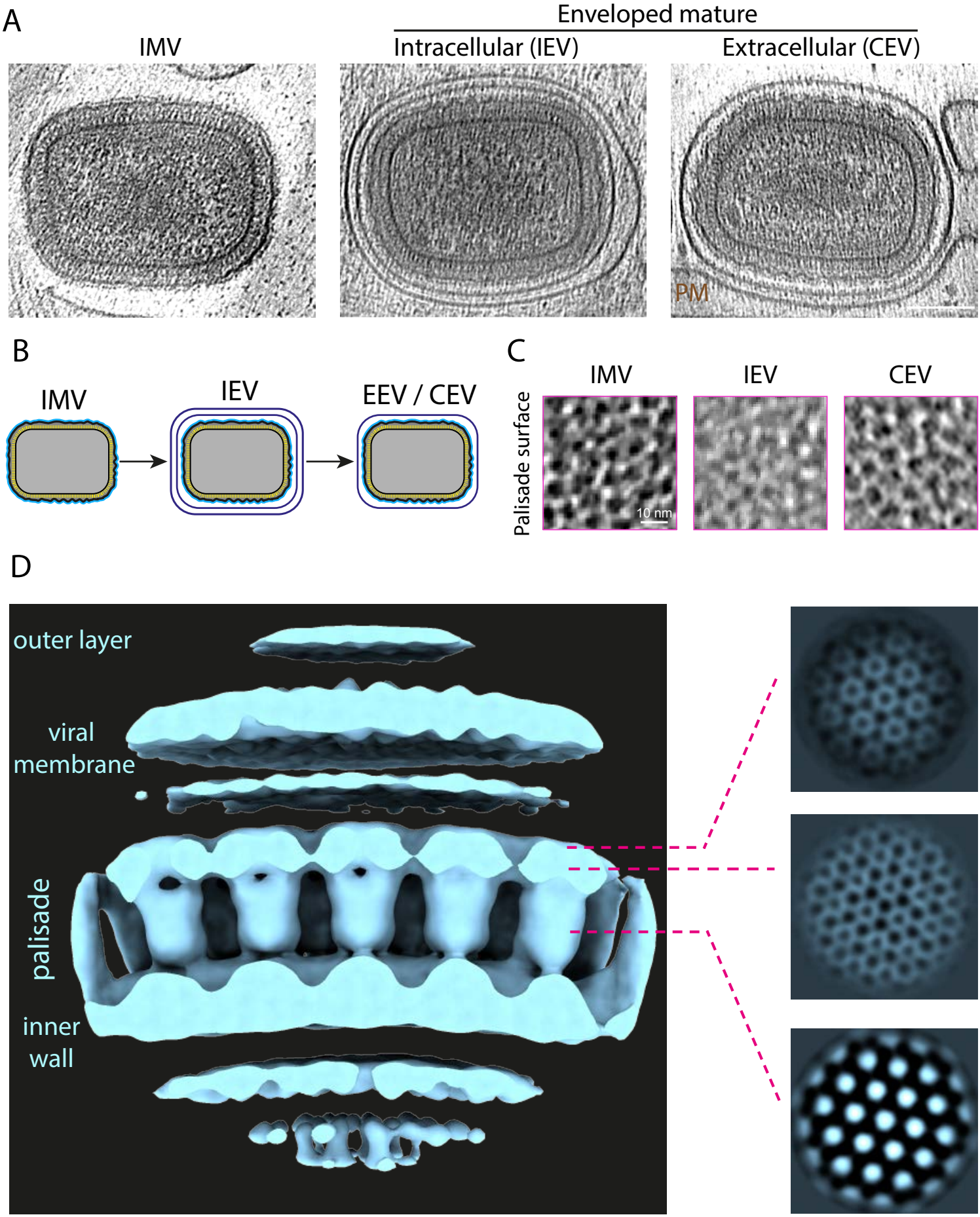
A
Enveloped mature
IMV
Intracellular (IEV)
Extracellular (CEV)
PM
B
IMV
IEV
EEV / CEV
C
IMV
IEV
CEV
Palisade surface
10 nm
D
outer layer
viral membrane
palisade
inner wall

Figure 6

A

	Immature virus (IV)		Intracellular mature virus (IMV)	
Approximate shape	Sphere		Triaxial ellipsoid	
Dimensions (nm)	Diameter	351.89 ± 2.88	Major axis	351.70 ± 3.31
			Intermediate axis	280.53 ± 3.66
			Minor axis*	198.04 ± 4.94
Perimeter (middle plane, (nm)	1106.39 ± 8.58		1087.75 ± 11.25	
Calculated volume (nm^3)	2.28×10^7		1.02×10^7	

B

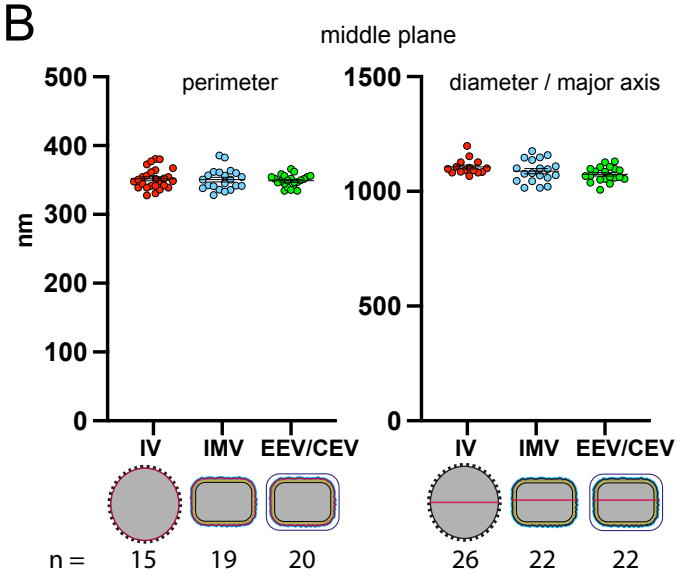

C

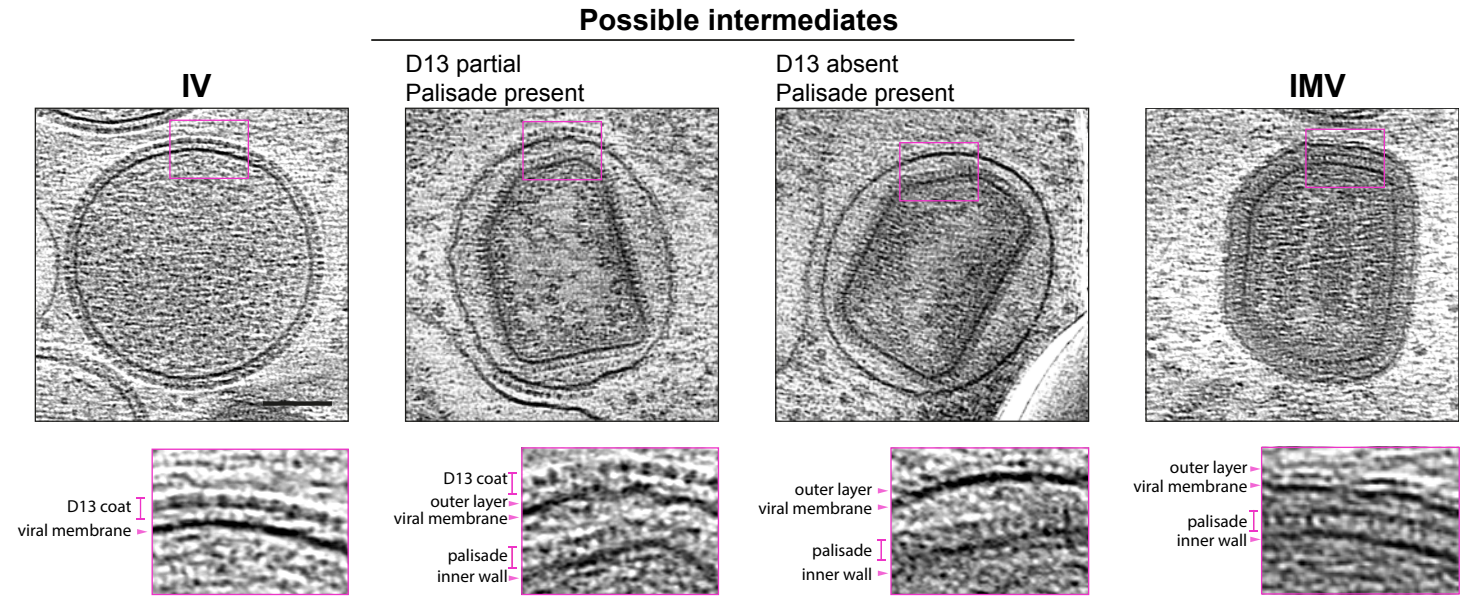

D

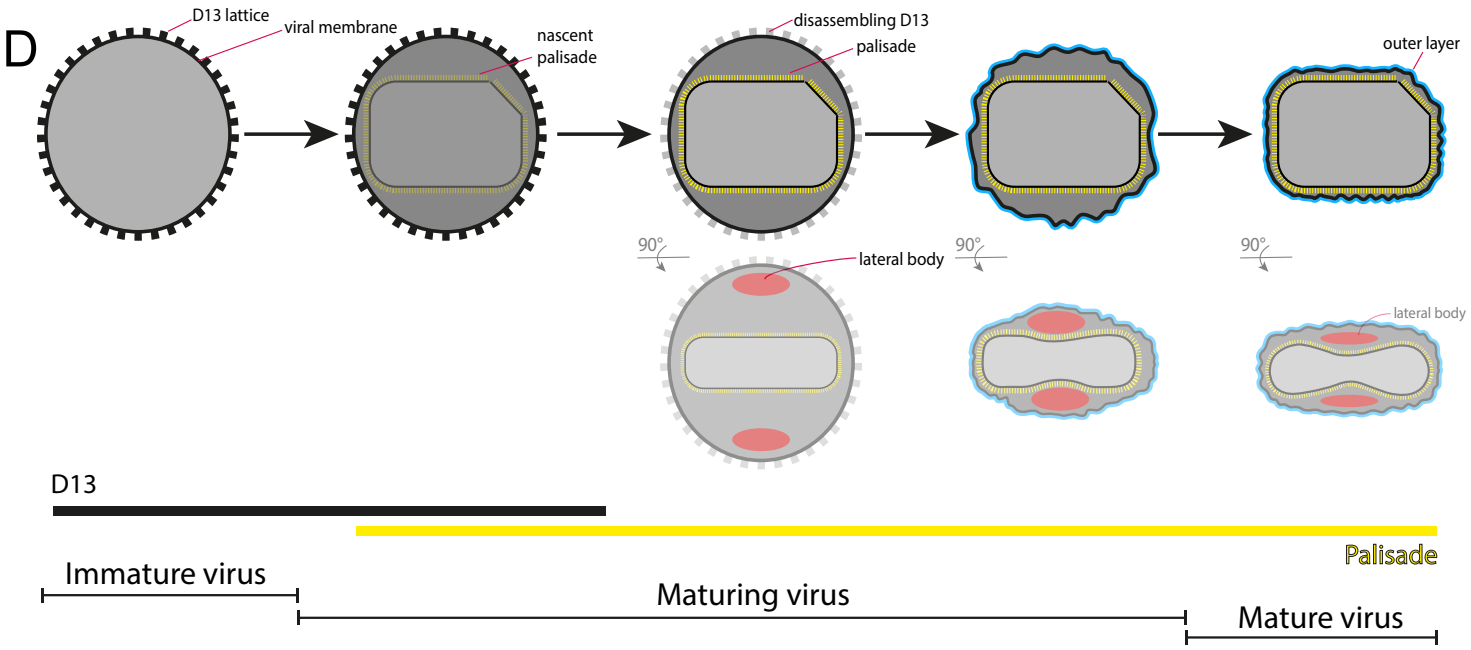

Figure 7

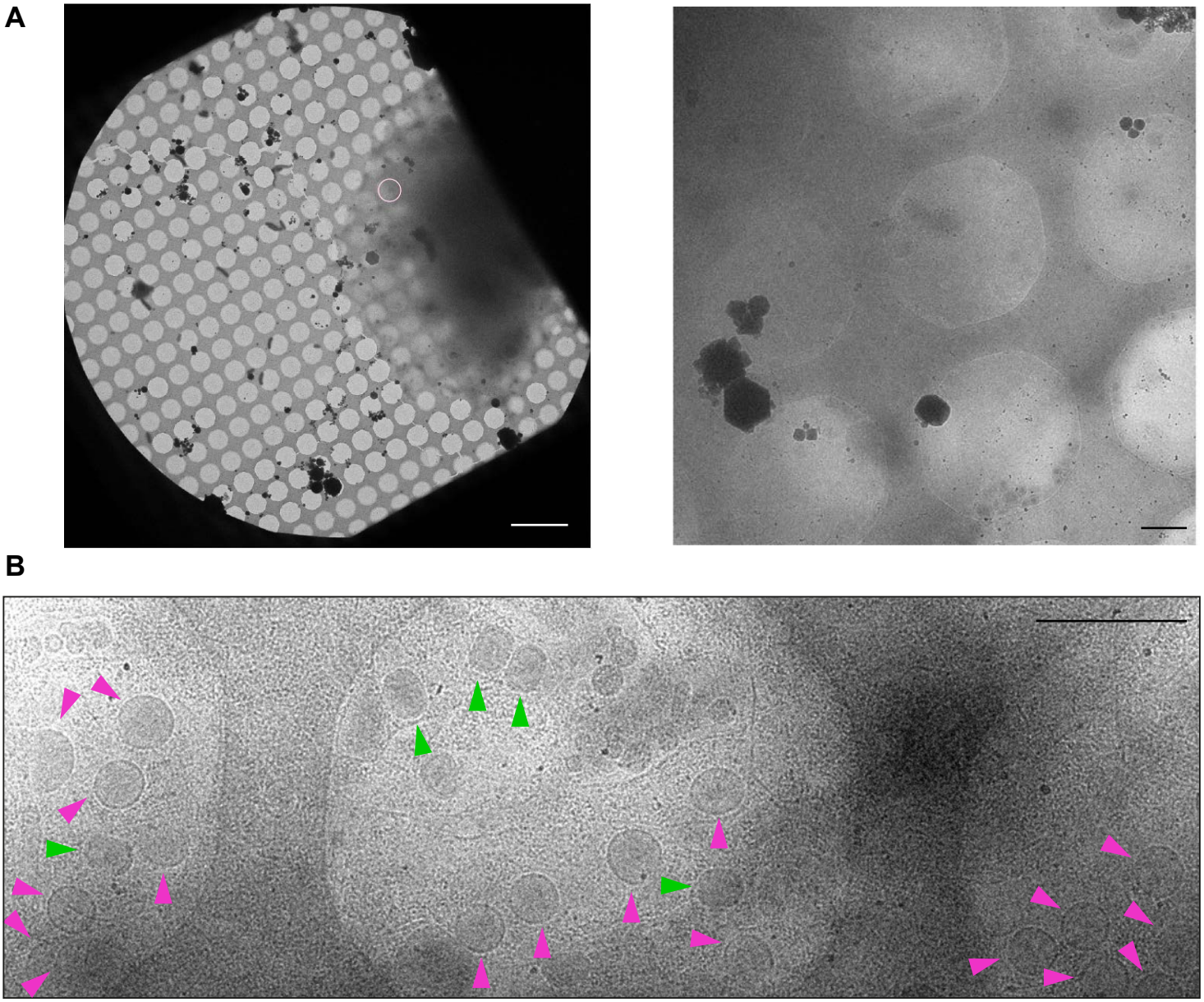

Supplementary Figure 1

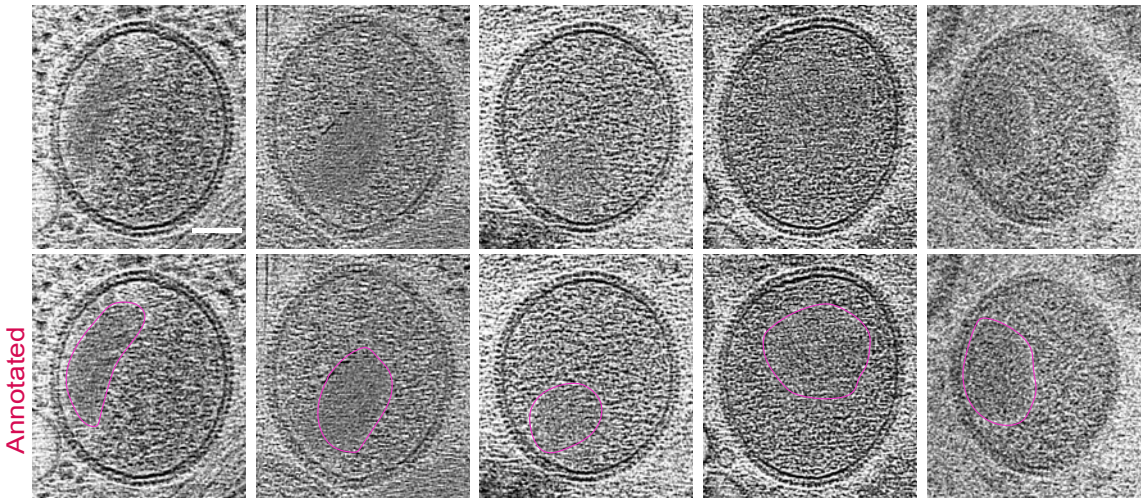

Supplementary Figure 2

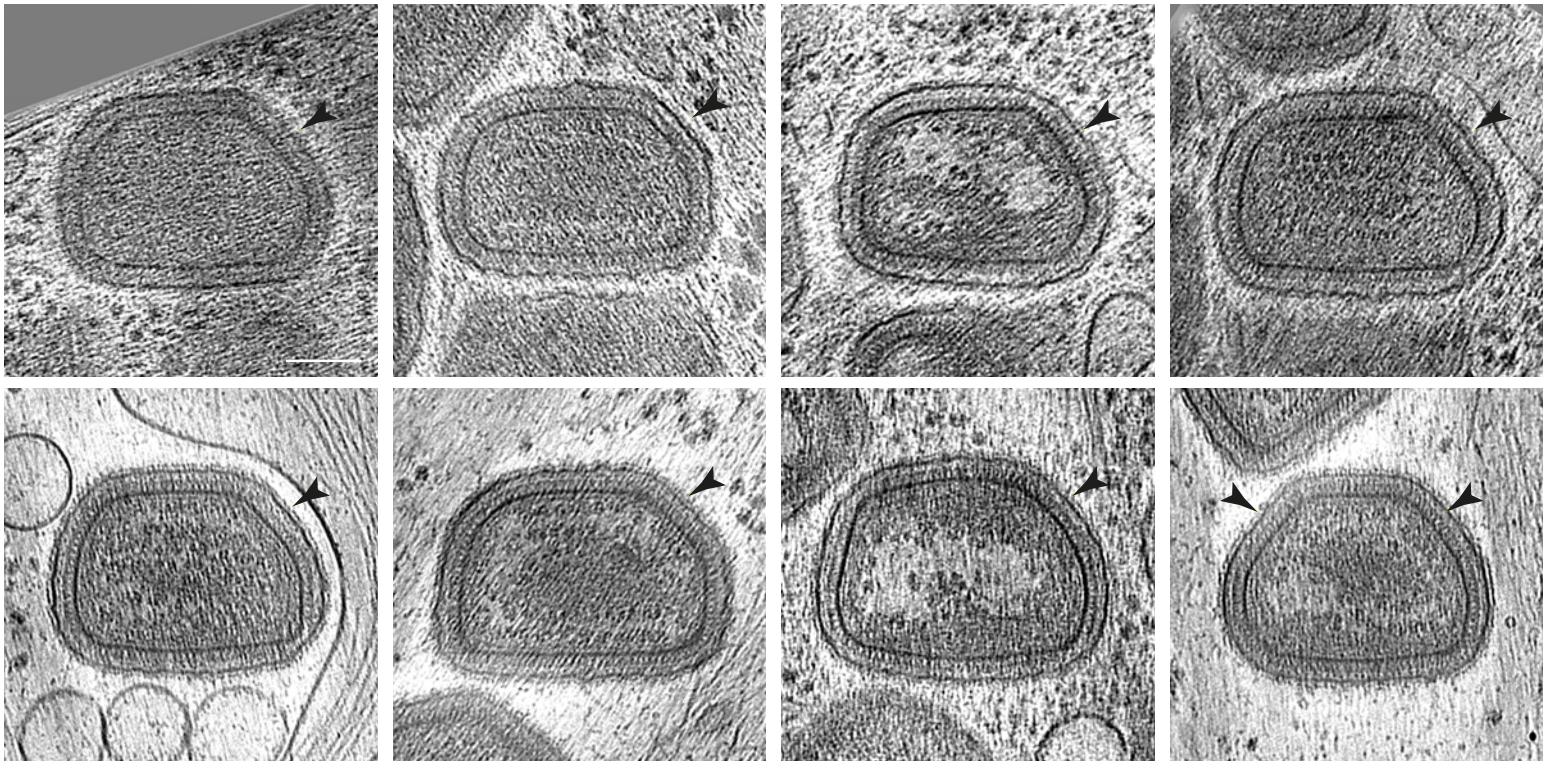

Cut corner : 48.9% No cut corner : 51.1% n = 94 IMV

Supplementary Figure 3

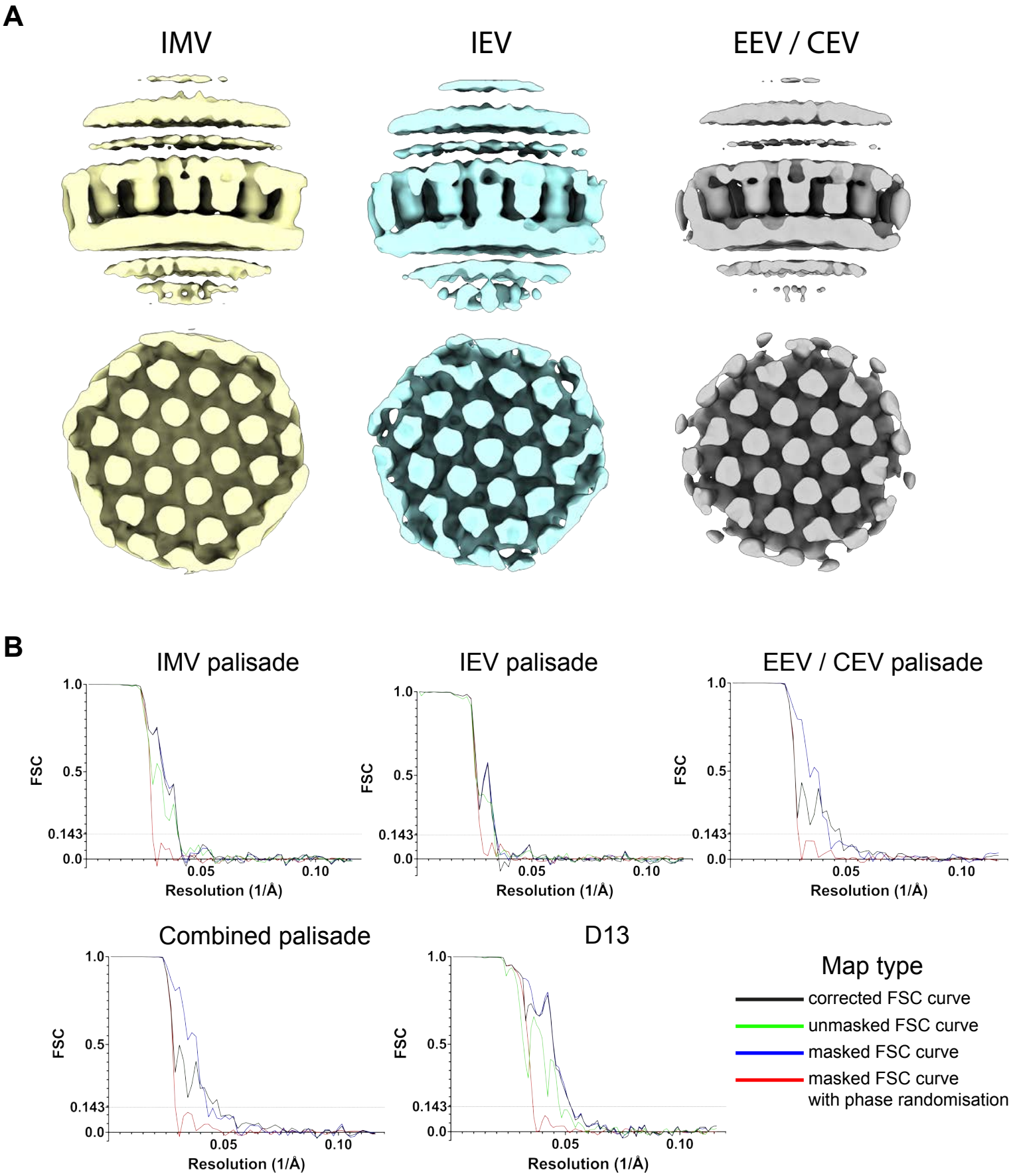

Supplementary Figure 4